JCB Journal of Cell Biology

ARTICLE

Completion of neuronal remodeling prompts myelination along developing motor axon branches

Mengzhe Wang[1], Tatjana Kleele[1], Yan Xiao[1], Gabriela Plucinska[1], Petros Avramopoulos[2,3], Stefan Engelhardt[2,3], Markus H. Schwab[4], Matthias Kneussel[5], Tim Czopka[1,6,9], Diane L. Sherman[7], Peter J. Brophy[7], Thomas Misgeld[1,8,9*], and Monika S. Brill[1,9*]

Neuronal remodeling and myelination are two fundamental processes during neurodevelopment. How they influence each other remains largely unknown, even though their coordinated execution is critical for circuit function and often disrupted in neuropsychiatric disorders. It is unclear whether myelination stabilizes axon branches during remodeling or whether ongoing remodeling delays myelination. By modulating synaptic transmission, cytoskeletal dynamics, and axonal transport in mouse motor axons, we show that local axon remodeling delays myelination onset and node formation. Conversely, glial differentiation does not determine the outcome of axon remodeling. Delayed myelination is not due to a limited supply of structural components of the axon–glial unit but rather is triggered by increased transport of signaling factors that initiate myelination, such as neuregulin. Further, transport of promyelinating signals is regulated via local cytoskeletal maturation related to activity-dependent competition. Our study reveals an axon branch–specific fine-tuning mechanism that locally coordinates axon remodeling and myelination.

Introduction

Myelin enables saltatory conduction and provides trophic support to the sheathed axons (Huxley and Stämpeli, 1949; Vabnick and Shrager, 1998; Yin et al., 2006; Simons and Trotter, 2007; Nave, 2010). In addition, recent observations in the central nervous system (CNS) indicate that myelin contributes to fine-tuning of neural circuits (Fields, 2015; Chang et al., 2016; Kaller et al., 2017). For instance, myelin sheaths and nodes of Ranvier, ion channel–enriched axon segments interspersed between myelin sheaths, show activity-dependent plasticity (Huff et al., 2011; Gibson et al., 2014; Mensch et al., 2015; Etxeberria et al., 2016; Korrell et al., 2019; Bacmeister et al., 2020) that appears to shape "patchy" myelination patterns in neocortex (Tomassy et al., 2014). While activity-regulated myelination is less studied in the peripheral nervous system (PNS; Stevens and Fields, 2000; Fields, 2015), in the PNS, the axon–glial unit is more accessible than in the CNS, and the signaling pathways governing peripheral myelination are better understood (Taveggia et al., 2010; Pereira et al., 2012; Grigoryan and Birchmeier, 2015). Thus, PNS development offers a privileged window into the intersection of axonal remodeling and myelin plasticity.

To capitalize on these advantages, we turned to a major site of PNS remodeling, the neuromuscular junction (NMJ). At mouse NMJs, axonal remodeling follows a predictable course during the first two postnatal weeks and can be followed at the single-axon-branch level (Lichtman and Sanes, 2003; Walsh and Lichtman, 2003). At birth, multiple motor axon branches innervate the same postsynaptic site (Tapia et al., 2012). Subsequently, all but one of these presynaptic inputs are eliminated by a two-step process that first involves activity-driven competition and then axon branch removal by cytoskeletal degradation (Buffelli et al., 2003; Brill et al., 2016) until lifelong innervation by a single axon is established (Tapia and Lichtman, 2012). Already during embryonic development, Schwann cells (SCs), the glia of the PNS, surround growing motor axons and accompany them to the target muscle (Jessen and Mirsky, 2005). SCs initiate myelination perinatally, after SCs have been sorted to sheath

[1]Institute of Neuronal Cell Biology, Technische Universität München, Munich, Germany; [2]Institute of Pharmacology and Toxicology, Technische Universität München, Munich, Germany; [3]German Center for Cardiovascular Research (DZHK), partner site Munich Heart Alliance, Munich, Germany; [4]Department of Neuropathology, University Hospital Leipzig, Leipzig, Germany; [5]University Medical Center Hamburg-Eppendorf, Center for Molecular Neurobiology (ZMNH), Institute for Molecular Neurogenetics, Hamburg, Germany; [6]Centre for Clinical Brain Sciences, University of Edinburgh, Edinburgh, UK; [7]Centre for Discovery Brain Sciences, University of Edinburgh, Edinburgh, UK; [8]German Center for Neurodegenerative Diseases (DZNE), Munich, Germany; [9]Munich Cluster of Systems Neurology (SyNergy), Munich, Germany.

*T. Misgeld and M.S. Brill contributed equally to this paper; Correspondence to Thomas Misgeld: thomas.misgeld@tum.de; Monika S. Brill: monika.leischner-brill@tum.de; T. Kleele's present address is École Polytechnique Fédérale de Lausanne, SB IPHYS LEB BSP 428 (Cubotron UNIL), Lausanne, Switzerland; G. Plucinska's present address is Guus Vleugelplantsoen 26, Utrecht, Netherlands; M.H. Schwab's present address is Department of Neuropathology, University Hospital Leipzig, Leipzig, Germany.

individual axon branches (Jessen and Mirsky, 2005; Monk et al., 2015; Rasband and Peles, 2015). Overall, myelination follows a proximal-to-distal gradient along motor axons, with myelination of terminal branches occurring last and asynchronously (Hildebrand et al., 1994; Yamamoto et al., 1996). This temporal correlation between axon–glial differentiation and cessation of developmental axon plasticity is a general feature across the nervous system and in the CNS can, e.g., be observed in visual cortex (Luo and O'Leary, 2005; McGee et al., 2005; Simons and Trotter, 2007). In the PNS, myelination onset is determined by the level of Neuregulin-1 (Nrg1) type III on the axonal surface. Nrg1 binds to glial ErbB2/3 receptors on SCs, leading to phosphorylation of downstream effectors, such as ERK1/2 and AKT (Garratt et al., 2000; Michailov et al., 2004; Taveggia et al., 2005; Iwakura and Nawa, 2013; Basak et al., 2015). While Nrg1 signaling is known to affect synapse development, the underlying signaling takes place at the NMJ itself, involving "terminal" nonmyelinating SCs rather than myelinating SCs along the axon (Loeb, 2003; Hayworth et al., 2006; Lee et al., 2016). Thus, whether the timing of branch-specific myelination also depends on local availability of Nrg1 and whether Nrg1 signaling is locally regulated to coordinate axon remodeling and myelination remain to be elucidated. Hence, using the NMJ as a model, we asked how axonal competition and axon–glial differentiation are coordinated at the single-branch level and what signaling mechanism is involved.

Results

Axon–glial differentiation is delayed on branches engaged in remodeling

To study the intersection of axon remodeling and myelination, we took advantage of a thoracic nerve-muscle explant, including the triangularis sterni muscle, which is uniquely suited to study the cell biological dynamics of single axon branches (Fig. 1 A; Kerschensteiner et al., 2008; Brill et al., 2013). During the second postnatal week, most NMJs transition from double to single innervation (abbreviated in the figures as din and sin, respectively), while myelin and nodes of Ranvier appear on terminal branches (Fig. 1 B). On three postnatal days (postnatal day 7 [P7], P9, and P11), we quantified the number of NMJs still engaged in synaptic competition using triangularis sterni muscles derived from *Thy1*-XFP mice, where motor axons are fluorescently labeled (Fig. 1, C and D; Feng et al., 2000). In parallel, we determined the state of axon–glial differentiation on singly innervating terminal branches based on the presence of immunostained Caspr1 (contactin-associated protein 1; Rasband and Peles, 2015) accumulations along a given terminal branch. We did not distinguish further between fully formed nodes (paranodes on both sides) and partially formed heminodes, resulting in a binary score ($Caspr^+$ vs. $Caspr^-$ terminal branches; Fig. 1, C and D). We observed a concomitant resolution of synaptic competition (i.e., decreasing percentage of doubly innervated synapses) and increasing paranodal formation on "winner" branches (Fig. 1 D). Finally, at P13, all NMJs established single innervation (100 ± 0%, n = 3 mice, 100 NMJs per animal), and all terminal branches started to form paranodes (100 ± 0%, n = 3 mice, 30 NMJs per animal). Next, we immunostained for myelin and other nodal components in *Thy1*-XFP mice at P9. In parallel to Caspr, nodal (voltage-gated sodium channel [Nav]), juxtaparanodal (contactin-2 [CNTN2]), and internodal (myelin protein zero [MPZ]) markers emerged on terminal branches (Fig. 1, E and F; Doyle and Colman, 1993). Thus, as myelin and nodal compartments coassemble rapidly (Girault and Peles, 2002; Schafer et al., 2006), we used Caspr immunostaining as a surrogate for overall axon–glial differentiation. Notably, when we focused on the branches still engaged in competition, we found significantly fewer branches immunopositive for emerging nodal structures, resulting in an overall delay of axon–glial differentiation of roughly 2 d (~33% of the full 6-d myelination period) compared with their winner siblings. This finding was consistent across all markers tested (Fig. 1 F). Thus, ongoing competition, and hence sustained plasticity, of terminal axon branches coincide with a transient stall of myelination and node formation. We considered two explanations for this delay: (1) slower assembly of structural components of the axon–glial unit or (2) reduced promyelinating signals. To disambiguate these scenarios, we analyzed the dynamics of node formation during axonal remodeling.

Axon remodeling delays the initiation, but not progress, of axon–glial differentiation

To measure the progress of axon remodeling, as well as the onset of node formation on individual motor axon branches, we characterized transgenic mice expressing GFP-tagged Caspr (Caspr-GFP; Fig. S1; Brivio et al., 2017) and generated mice expressing the β1 subunit of the Nav tagged with GFP (β1-Nav-GFP; Fig. S1), both under control of the *Thy1* promotor. In both lines, progress of synapse elimination and onset of node formation were unchanged compared with WT littermates at P9 (Fig. S1 legend). We assessed the paranodal/nodal protein dynamics by FRAP (see Materials and methods) and related the recovery rate to axonal competition status in β1-Nav- or Caspr-GFP crossed to *Thy1*-OFP3 mice (Brill et al., 2011). GFP-positive clusters forming heminodes were photobleached to approximately one third of their original fluorescence intensity (33 ± 3%, n = 135 nodes in 46 mice) and visualized again 3 h later. The recovery was normalized to nonbleached control nodes in the same field of view to account for imaging-related fluorescence loss (Fig. 2, A and C). Surprisingly, at P9–P11, we found significantly higher recovery rates of β1-Nav- or Caspr-GFP on competing doubly innervating branches compared with singly innervating ones (Fig. 2, B and D), suggesting that once initiated, node formation progressed swiftly. We also found an age-dependent decline (Rios et al., 2000). Recently established nodal structures recover much faster than mature ones (sin P9–P11 vs. sin 6 wk; Caspr-GFP ~4.3-fold; β1-Nav-GFP ~4.4-fold; Zhang et al., 2012). At the same time, P9–P11 nodes in proximal positions (stem; Fig. 2, B and D) resembled distal mature (i.e., 6 wk) nodes, consistent with the known myelination gradient (Hildebrand et al., 1994). Hence, our data favor a mechanism where axonal competition delays the initiation, but not progress, of axon–glial maturation. However, myelination and node formation are still initiated on a subset of competing, doubly innervating axon branches (cf.

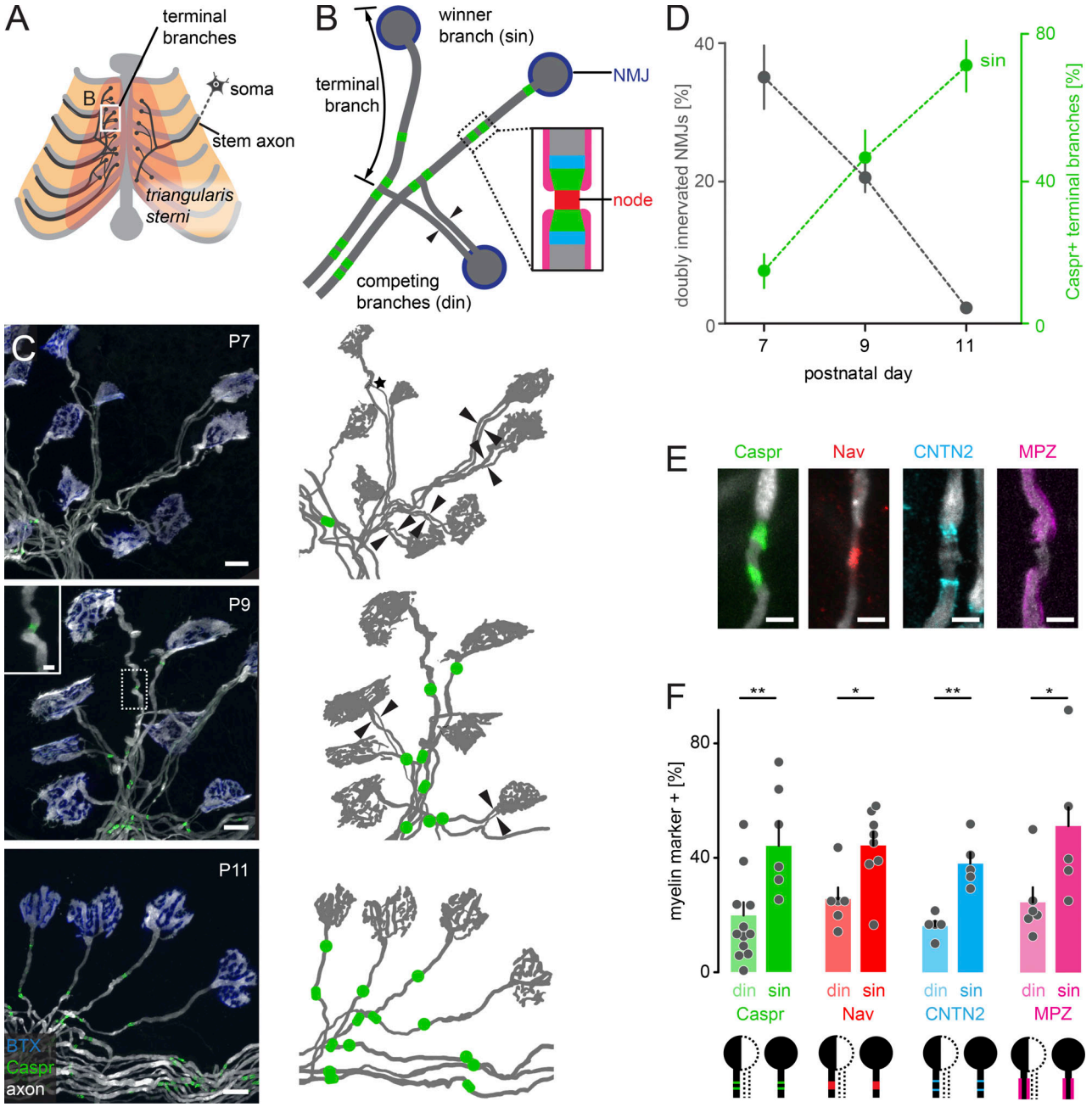

Figure 1. **Myelination coincides with axon remodeling during the second postnatal week. (A)** Schematic of thoracic nerve-muscle explant indicating anatomy of motor axons (dark gray), including the stem axon in the intercostal nerve, soma (motor neuron cell body in spinal cord), triangularis sterni muscle (pink), and sternum and ribs (light gray). The boxed area of terminal branches is schematized in more detail in B. **(B)** Schematic of terminal branches of motor neurons (dark gray), postsynaptic AChRs (NMJ; blue). Arrowheads point to two competing branches leading to the same NMJ; sin, winner branch. Regions of nodes of Ranvier include paranodes (green), node (red), and juxtaparanodes (cyan). SCs myelinate axons in internodal regions (magenta). **(C)** P7, P9, and P11 triangularis sterni muscles of *Thy1*-YFP16 mice (axon, white) immunostained for Caspr (green) and postsynaptic AChRs (BTX, blue). Inset shows an emerging paranodal Caspr cluster at P9. Corresponding schematics to the right show axons (gray) and Caspr-positive paranodes (green). Arrowheads point to two axons leading to the same NMJ. **(D)** Quantification of the percentage of doubly innervated NMJs at P7, P9, and P11 ($n \geq 5$ mice, ≥100 NMJs per animal, gray) and the percentage of Caspr-positive terminal branches among singly innervated NMJs ($n \geq 5$ mice, ≥100 NMJs per animal, gray) and the percentage of Caspr-positive terminal branches among singly innervated NMJs ($n \geq 7$ mice, ≥30 branches per animal, green). **(E)** Nodes of Ranvier and myelin components show immunostaining for Caspr (green, paranode), Nav (red, nodal region), CNTN2 (cyan, juxtaparanode), and MPZ (magenta, myelin) in single terminal axon branches of Thy1-XFP mice (axons, white). **(F)** Quantification of the percentage of myelin initiation on winner (singly innervating [sin]) or competing (doubly innervating [din]) terminal axon branches for Caspr (green), Nav (red), CNTN2 (cyan), or MPZ (magenta; $n \geq 5$ mice per group, ≥50 branches). Data represent mean ± SEM (D) or mean + SEM (F). *, $P < 0.05$; **, $P < 0.01$; Mann–Whitney test. Scale bars represent 10 µm (C, overview) and 2 µm (C, inset, and E).

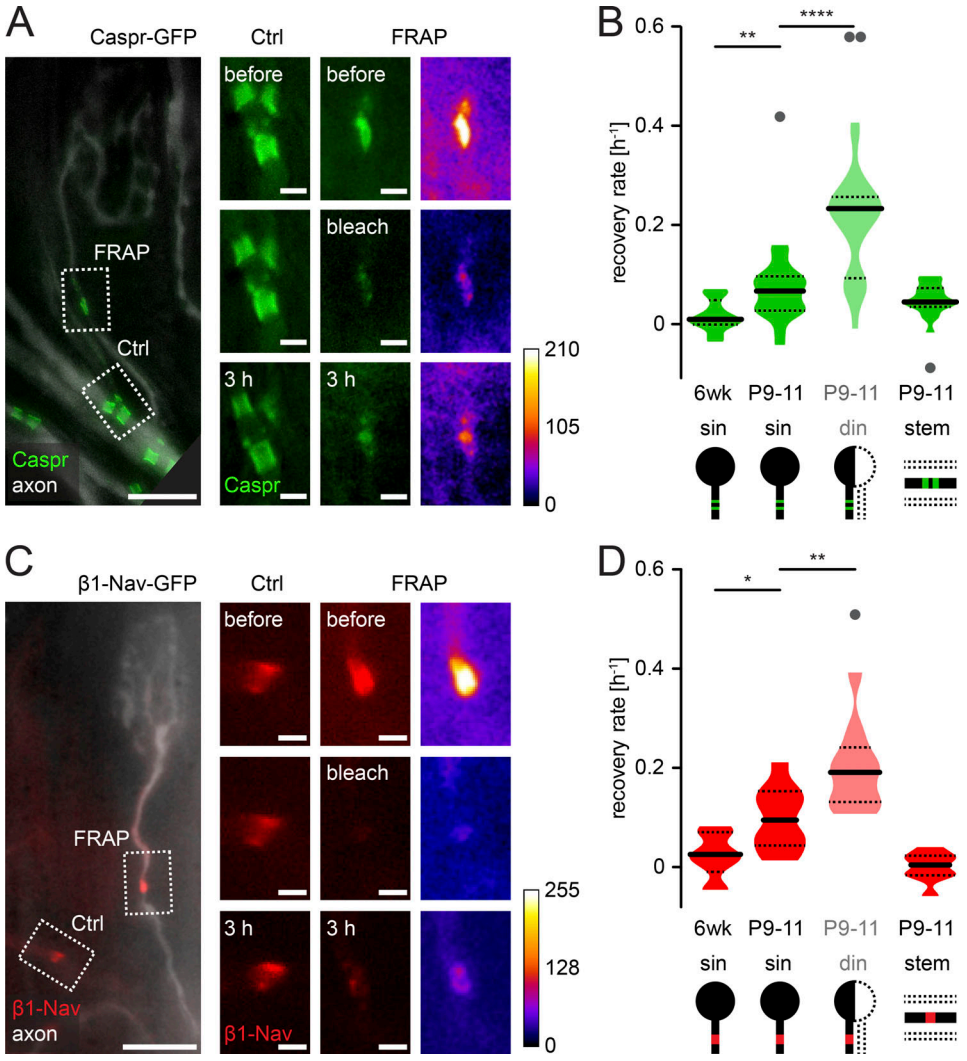

Figure 2. **Nodes on competing branches are immature compared with those on winner branches. (A)** Live image of motor axons in P11 *Thy1*-Caspr-GFP (green) × *Thy1*-OFP3 (axon, white) nerve-muscle explant; dashed boxes indicate location of control (Ctrl) and photobleached (FRAP) nodes. Images on the right are taken before, directly after photobleaching, and 3 h later. Fire lookup table on the right. **(B)** Quantification of Caspr-GFP recovery rate comparing winner branches (sin) of different developmental ages (6 wk vs. P9–P11) and different competition status at the same developmental age (P9–P11 sin, din, stem; $n \geq 13$ axons, ≥10 mice per group). **(C)** Live image of axon branches in P11 *Thy1*-β1-Nav-GFP (red) × *Thy1*-OFP3 (axon, white) nerve-muscle explant; dashed boxes and images on right as in A. **(D)** Quantification of β1-Nav-GFP recovery rate as in B ($n \geq 9$ axons, ≥5 mice per group). din, doubly innervating competing branch; sin, singly innervating winner branch. Data represent mean + SEM. *, $P < 0.05$; **, $P < 0.01$; ****, $P < 0.0001$; Mann–Whitney test; outliers identified with Tukey's test. Scale bars, 10 µm (A and C, overview) and 2 µm (insets).

Fig. 1 F). Thus, we wondered whether disparate progress of axon–glial maturation influences the competition outcome.

Axon–glial maturation does not convey an advantage in synaptic competition

To address the effect of a branch's axon–glial maturation status on competition, we related initiation of node formation to synaptic territory (i.e., the fraction of an NMJ that a terminal branch innervates). Synaptic territory is a well-established indicator of probable competition outcome (Gan and Lichtman, 1998; Walsh and Lichtman, 2003; Brill et al., 2016). We determined synaptic territory using the Brainbow approach to individually color motor units (*ChAT*-Cre x *Thy1*-Brainbow-1.1; Fig. 3 A; Livet et al., 2007; Rossi et al., 2011) and immunostained for Caspr to reveal node formation along terminal branches at P9. Throughout all stages of axonal competition (1–99% territory), less than ∼20% of the branches were Caspr positive, and there was no correlation of myelination onset to synaptic territory (Fig. 3 B). However, once competition was resolved, Caspr was present on ∼50% of the singly innervating terminal branches (100% territory; χ^2 test, 1–99% vs. 100%, $P < 0.0001$, $n = 749$ axon branches in 45 mice; Fig. 3 B), suggesting a swift lift of the brake on axon–glial differentiation once competition was resolved. This lack of correlation contrasts with other cell biological features of terminal branches, including cytoskeletal stability, organelle transport, or caliber, which are highly correlated to synaptic territory (Keller-Peck et al., 2001; Brill et al., 2016). Moreover, the measured distribution of node formation patterns on

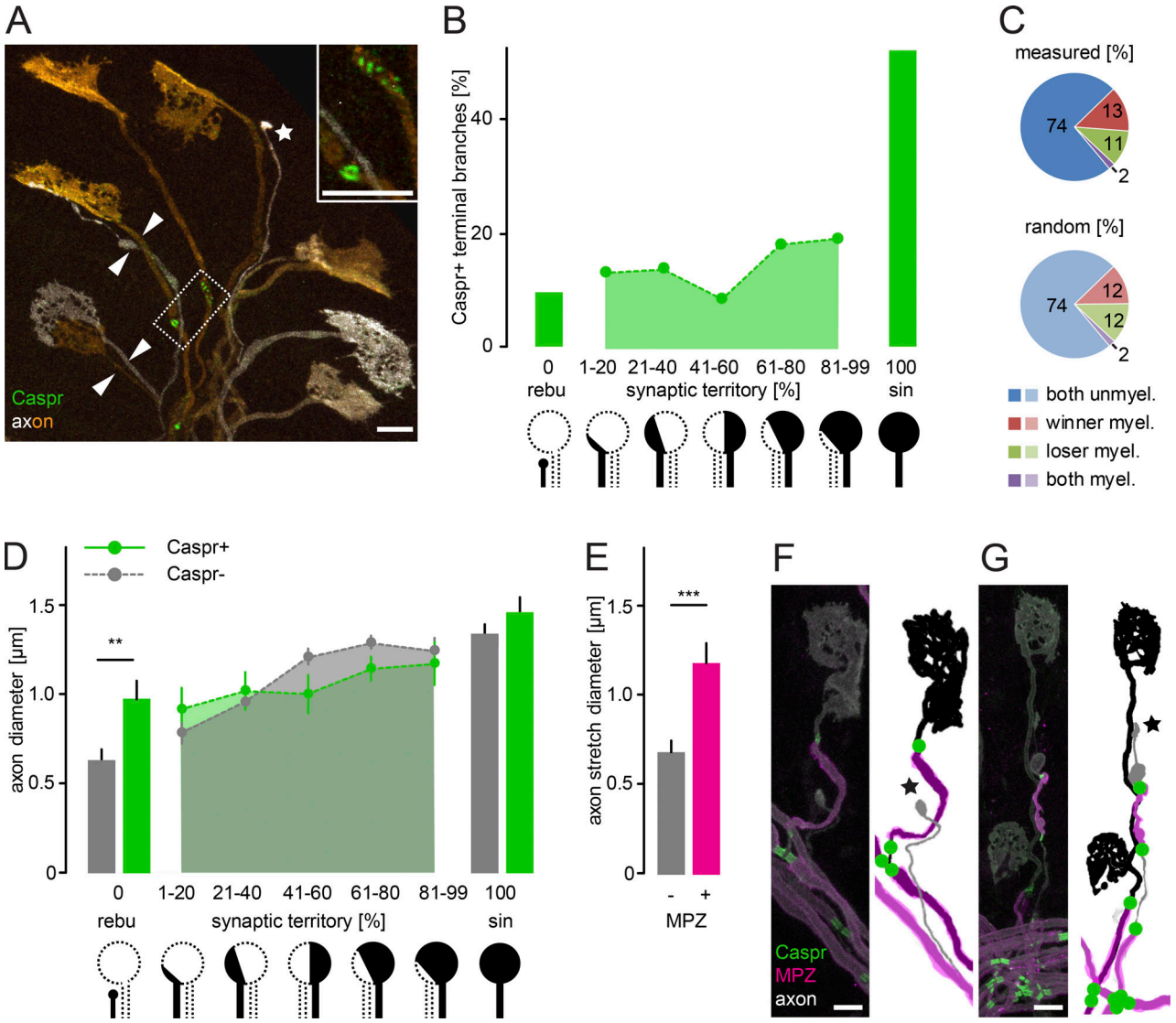

Figure 3. **Myelination of competing branches neither biases competition nor reflects axon diameter. (A)** Image of a fixed triangularis sterni muscle of a *ChAT*-IRES-Cre × *Thy1*-Brainbow-1.1 mouse. Motor units labeled with distinct fluorescence (axon, orange and white) and immunostained for Caspr (green); arrowheads point to competing branches, and asterisk marks a pruning axon. Inset shows enlarged dashed box with emerging dotty and more mature paranodal structures. **(B)** Quantification of Caspr immunostaining versus synaptic territory of competing branches ($n \geq 78$ axons per group from a total of 69 mice). **(C)** Graph of measured myelination patterns on paired competing branches versus the calculated distribution assuming random myelin initiation. Winner is an axon branch ≤50% territory, while loser is ≥50% territory. **(D)** Quantification of an axon's diameter versus its synaptic territory in axon branches either with (green) or without Caspr immunostaining (gray; n v 10 axons, v7 mice per group). **(E)** Quantification of the diameter of stretches on retreating axons with (magenta) or without MPZ-immunostaining (gray; n v 8 axons, ≥4 mice per group). **(F and G)** Images of *Thy1*-XFP terminal branches (axons, white) stained for Caspr (green) and MPZ (magenta). Schematics to the right depict a myelinated winning branch (black) versus a pruning axon (gray; star) without nodes (F) and a rare example of a myelinated retreating branch (gray; star) and its winning MPZ- and Caspr-negative competitor (black; G). rebu, retraction bulbs; sin, winner axons; (un)myel., (un)myelinated. Data represent mean ± SEM. **, $P < 0.01$; ***, $P < 0.001$, Mann–Whitney test. Scale bars, 10 µm (A, F, and G).

competing axons, such as the fraction of NMJs where node formation had started on the winning branch (51–99% territory), the losing branch (1–49% territory), or neither of the competing branches, matched a random binomial distribution (14% din myelinated across 1–99% territory, $n = 520$ din NMJs in 35 mice; Fig. 3 C). This, however, does not rule out caliber as a central driver of node formation onset, as known for other PNS settings, where 1 µm represents a critical threshold for myelination (Voyvodic, 1989; Peters et al., 1991). Therefore, we analyzed the diameter of competing branches with or without emerging nodes (Fig. 3 D) and found no difference between the groups during all stages of competition. We even found (albeit rarely) partially myelinated axon branches that lost against a nonmyelinated competitor (Fig. 3, F and G). Only in retreating branches were the pruning axons with emerging nodes significantly thicker than their unmyelinated counterparts (Fig. 3 D), possibly due to the protective effect of myelin on axonal structures, as axon stretches covered by MPZ are significantly thicker than MPZ-negative stretches along the same retreating branches (Fig. 3 E; Nave, 2010). Hence, at the NMJ, axon–glial

differentiation neither decides competition nor prohibits axon pruning (McGee et al., 2005). Together, the data suggest a unidirectional relationship, with ongoing axon remodeling delaying axon–glial maturation, but not the converse. Next, we wanted to test which phase of synapse remodeling impacted axon–glial maturation to narrow down possible underlying signaling mechanisms.

Suspending competition, but not late branch removal, delays axon branch myelination

Synapse remodeling can be divided into several phases (Kano and Hashimoto, 2009; Turney and Lichtman, 2012), with an early activity-dependent competition phase driven by neurotransmission (Buffelli et al., 2003) followed by a late execution phase involving cytoskeletal breakdown and glial engulfment (Bishop et al., 2004; Brill et al., 2016). First, we intervened during competition by irreversibly blocking postsynaptic acetylcholine receptors (AChRs) using unilateral thoracic injection of α-bungarotoxin (BTX; Akaaboune et al., 1999; Kummer et al., 2004) of P7 *Thy1*-XFP mice (Fig. 4 A). Paired analysis on contra- versus ipsilateral triangularis sterni muscles 2 d later (P9; Fig. 4, B and C) revealed that more multiple innervation was maintained after BTX injection (Fig. 4 D; Loeb et al., 2002; Buffelli et al., 2003). Notably, the number of Caspr-positive winner branches (sin) was significantly reduced (Fig. 4 E), suggesting that blocking neurotransmission delays the initiation of node formation. At the same time, we did not measure a change of axonal SC number or internode or terminal branch length after BTX treatment (Fig. S2, A–D). Under physiological conditions, the number of SCs slightly increases as competition resolves (indicated by reduced SC length; Fig. S2, E and F). We therefore hypothesized that BTX injection maintained terminal branches in a more juvenile state. Thus, we turned to the microtubular cytoskeleton as an important indicator for axonal maturation, since microtubular mass increases as the branch gains synaptic territory (Brill et al., 2016). The initiation of myelination correlates with an increase in tubulin content (Fig. S2 G and H). Following BTX injection, microtubular mass on winner axons (sin) decreased to ∼60%, while competing axons (din) were not affected (Fig. 4, F and G). This hints at the possibility that the delayed node formation following transmission block is due to reduced microtubular mass.

To manipulate axonal microtubules, we genetically deleted spastin, a microtubule-severing enzyme (spastin KO), where we confirmed a delay in axon branch removal (Fig. 4, H–J; Brill et al., 2016). Indeed, loss of spastin led to accelerated node formation in competing axons (din) compared with WT (Fig. 4 K). That this represented a cell-autonomous effect in motor neurons was corroborated by inducing subset deletion in conditional spastin$^{fl/fl}$ × TdTomato reporter mice (Brill et al., 2016) using a Cre-encoding adeno-associated virus (AAV; AAV9-*CMV*-iCre; Fig. S3). While we again found delayed axon remodeling (Brill et al., 2016), node formation was now accelerated on competing branches (Fig. S3 C), where TdTomato expression indicated spastin deletion. Overall, microtubular mass was increased in spastin-deleted terminal axon branches (Fig. 4, L and M; Brill et al., 2016), while axonal caliber was unaffected (Fig. S3 D), contrasting the increase in nodal formation specifically on competing branches. This suggests that the microtubular cytoskeleton is the limiting factor to initiate node formation in competing branches, but not on winner axons, perhaps arguing for a two-component system, where each can be limiting in different stages. Moreover, the divergent axon–glial differentiation outcomes of postsynaptic block versus spastin deletion, which both delay remodeling, points to a mechanism that is blocked by ongoing activity-dependent competition but can be overcome by increasing microtubular mass. As the microtubular cytoskeleton sustains axonal transport (which requires tracks and cargoes), we next tested if reducing anterograde transport would affect local initiation of axon–glial differentiation.

Local axonal transport regulates terminal branch myelination during remodeling

To reduce transport in motor neurons, we overexpressed the cargo-binding domain (CBD) of kinesin-1 heavy chain (KHC), a key molecular motor driving anterograde transport (Hirokawa et al., 2009). This results in a dominant-negative mutant (KHC-CBD), which still binds cargoes but lacks the motor domain and competes with endogenous kinesin-1, thus impairing transport of organelles and nodal components in vitro (Cai et al., 2005; Barry et al., 2014). To test the efficacy of this approach in vivo, we turned to zebrafish as an easily accessible model for assaying effects of myelination-regulating signals (Czopka and Lyons, 2011). We used the Gal4/UAS system to transiently coexpress *UAS*-GFP-KHC-CDB and *UAS*-mitoTagRFP-T in Rohon–Beard sensory neurons, in which mitochondrial transport can be easily monitored (Plucińska et al., 2012). KHC-CBD overexpression in this system substantially reduced mitochondrial transport per minute (reduction from 0.61 ± 0.11 in control to 0.10 ± 0.02 in anterograde and 0.28 ± 0.04 to 0.10 ± 0.04 in retrograde direction at 2 d postfertilization [dpf]; $P < 0.01$, Mann–Whitney test, $n \geq 4$ zebrafish per group, ≥4 axons). We then analyzed spinal motor neurons, which start to be myelinated at 3 dpf in zebrafish (D'Rozario et al., 2017). To down-regulate axonal transport while monitoring myelination progress, we expressed GFP-KHC-CBD or GFP alone under the neuronal *cntn1b* promoter in Tg(mbp:RFP) zebrafish, where all compacted internodes are fluorescently labeled by a membrane-targeted RFP (Fig. S4, A–E; Auer et al., 2018). On 6 dpf, axon length in Tg(mbp:RFP) zebrafish injected with cntn1b-GFP-KHC-CBD was similar to controls (Fig. S4 F), but strikingly, the myelinated axon length was only half compared with controls (Fig. S4 G). This supports the notion that PNS myelination depends on axonal transport.

We next probed whether this was true in murine motor axons during remodeling. In *Thy1*-β1-Nav-GFP animals, emerging β1-Nav-GFP clusters correlate with higher anterograde particle transport in terminal branches (Fig. 5). Among all β1-Nav-GFP-positive branches, winner axons (sin) had the highest anterograde transport rate (Fig. 5 B). Together, this is in line with our previous observation that microtubular mass correlates with node formation (Fig. S2 H). We then injected an AAV9 encoding KHC-CBD and iCre under control of the neuronal human synapsin promoter (AAV9-*hSyn*-iCre-p2a-KHC-CBD) into neonatal mice (Fig. 5 A). In AAV-injected *Thy1*-β1-Nav-GFP × TdTomato

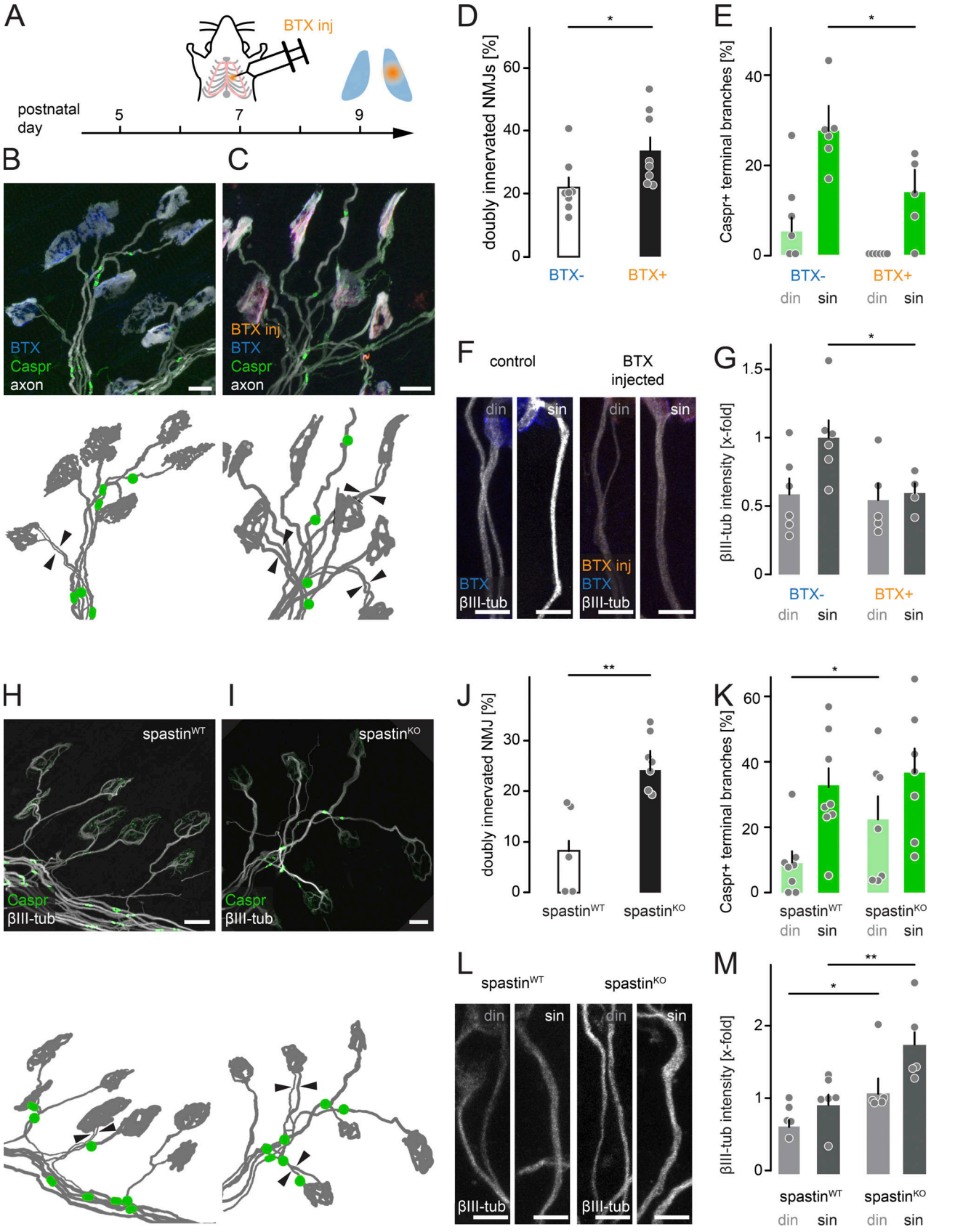

Figure 4. **Neurotransmission and spastin differentially affect myelination and microtubular mass. (A)** Schematic of experimental design. *Thy1*-YFP16 mice were unilaterally injected with BTX ("BTX inj", orange) into the thoracic wall at P7, resulting in local blockade of AChRs. Fixed ipsi- and contralateral muscles are post hoc stained at P9 with BTX (blue) and immunostained for Caspr (green). **(B and C)** Contralateral control muscle (B) and ipsilateral BTX-

injected muscle (C) showing axons (*Thy1*-YFP16, white), Caspr immunostaining (green), post hoc stained BTX (blue), and injected BTX (orange). Schematics below depict motor neurons (gray) and Caspr paranodes (green); arrowheads point to two competing axons leading to the same NMJ. **(D)** Quantification of doubly innervated NMJs at P9 following BTX injection (n = 8 mice, ≥50 axons per animal). **(E)** Quantification of Caspr-positive competing (din) and winner (sin) axon branches from BTX-injected muscles versus controls ($n \geq 5$ mice, ≥32 axons per side of animal). **(F)** Images of competing (din) and winner (sin) terminal branches following BTX injection (orange) and post hoc staining at P9 with BTX (blue) and βIII-tubulin (white). **(G)** Quantification of βIII-tubulin intensity (x-fold normalized to *Thy1*-YFP16; $n \geq 5$ mice, $n \geq 20$ axons per side of animal). **(H and I)** P9 triangularis sterni muscle of littermate WT (H) and spastin KO (I) mice. Axons immunostained for Caspr (green) and βIII-tubulin (white). Corresponding schematics below show axons (gray) and Caspr-positive paranodes (green). Arrowheads point to two axons innervating the same NMJ. **(J)** Quantification of doubly innervated NMJs in P9 spastin KO animals compared with WT littermates ($n \geq 5$ mice, $n \geq 70$ axons per animal). **(K)** Quantification of Caspr-positive terminal branches in P9 spastin KO compared with WT littermates ($n \geq 7$ mice, $n \geq 33$ axons per animal). **(L)** Images of competing (din) and winner (sin) terminal branches in spastin WT and KO littermates, immunostained for βIII-tubulin (white). **(M)** Quantification of βIII-tubulin intensity (x-fold normalized to *Thy1*-YFP16) in spastin KO versus WT littermates ($n \geq 5$ mice, $n \geq 13$ axons per animal). din, competing axons; sin, winner axons. Data represent mean + SEM. Mann–Whitney test. *, P < 0.05; **, P < 0.01. Scale bars represent 10 µm (B, C, H, and I) and 5 µm (F and L).

reporter mice, we found a significant reduction in β1-Nav-GFP anterograde transport, while retrograde rates were unaffected (Fig. 5 B). Notably, the onset of node formation was significantly delayed in reporter-positive branches compared with negative ones, which served as internal controls (Fig. 5, C and D). This points to a transport-delivered signal, which locally times the onset of axon–glial differentiation of terminal axon branches.

Local disparity of promyelinating factors in terminal branches correlates with competition status

Nrg1 type III is a candidate for a transported promyelination signal, as this signaling factor locally needs to reach a critical threshold to initiate axon–glial differentiation (Taveggia et al., 2005; Nave and Salzer, 2006; Birchmeier and Nave, 2008; Velanac et al., 2012) by activating downstream effectors in SCs such as ERK1/2 and AKT (Ogata et al., 2004; Taveggia et al.,

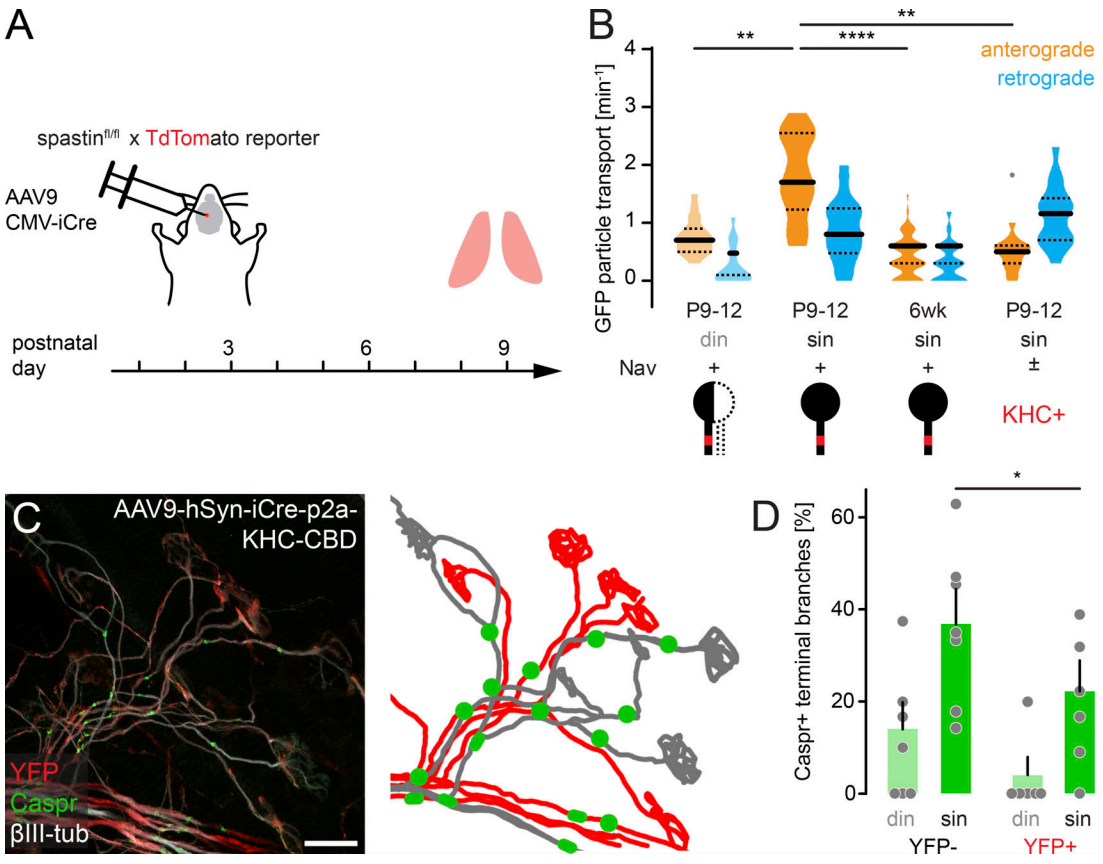

Figure 5. **Axonal transport limits myelination onset in terminal motor axon branches. (A)** Schematic of experimental design. AAV9-*hSyn*-iCre-p2a-KHC-CBD was injected at P2 into the third ventricle of YFP reporter mice. Muscles were analyzed at P9. **(B)** Quantification of axonal GFP particle transport in β1-Nav-GFP animals ($n \geq 5$ mice per group, $n \geq 16$ axons). **(C)** Image of AAV9-hSyn-iCre-p2a-KHC-CBD-injected P9 triangularis sterni muscle of a YFP reporter mouse immunostained for Caspr (green) and βIII-tubulin (white). KHC-CBD is overexpressed in iCre-induced recombined YFP reporter–positive axons (red). Schematic on the right depicts YFP-positive (red) and YFP-negative motor units (gray) and Caspr paranodes (green). **(D)** Quantification of Caspr immunostaining on YFP-negative and YFP-positive terminal axon branches at P9 ($n \geq 5$ mice per group, $n \geq 39$ axons per mouse). din, competing axons; sin, winner axons. Data represent mean + SEM. *, P < 0.05; **, P < 0.01; ****, P < 0.0001; Mann–Whitney test. Outlier determined by Tukey test. Scale bar, 20 µm (C).

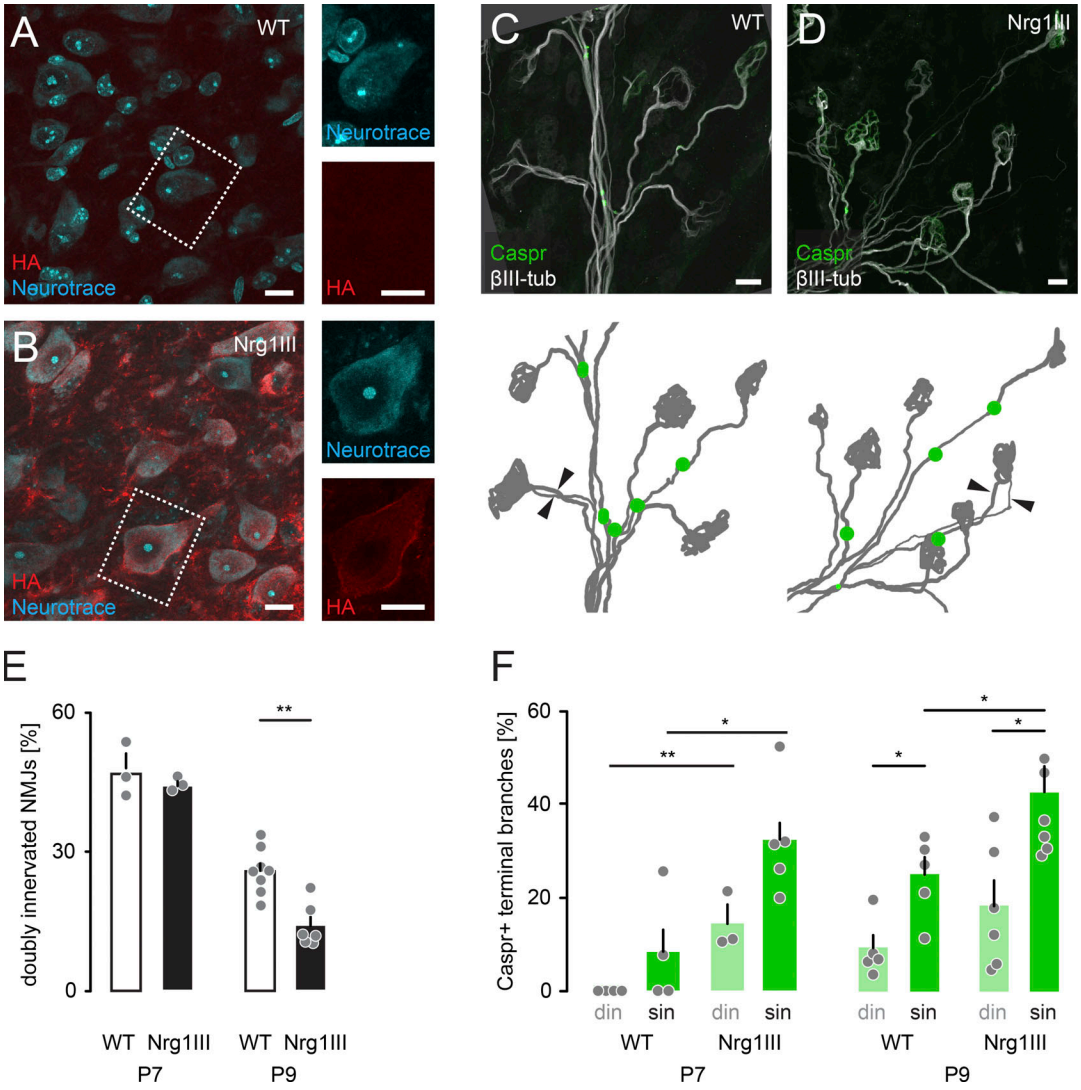

Figure 6. **Nrg1 type III transgenic mice show premature myelination initiation. (A and B)** P9 spinal cord of WT control (A) and *Thy1*-Nrg1 type III-HA (B) littermates. Sections stained for HA-tag (red) and neurotrace (cyan). Dashed boxes enlarged on the right show magnified single channels of neurotrace (cyan) and HA staining (red). **(C and D)** Confocal images of P9 triangularis sterni muscles from WT (C) and Thy1-Nrg1 type III-HA littermates (D) immunostained for βIII-tubulin (white) and Caspr (green). Schematics below show motor neurons (gray) and Caspr paranodes (green). Arrowheads point to two axons leading to the same NMJ. **(E and F)** Quantification of the percentage of doubly innervated NMJs (E) and Caspr-positive terminal branches (F) in P7 and P9 WT versus transgenic *Thy1*-Nrg1 type III littermates (E, $n \geq 3$ mice per genotype, ≥99 axons per animal; F, $n \geq 3$ mice per genotype, ≥40 axons per animal). din, competing axons; sin, winner axons. Data represent mean + SEM. *, $P < 0.05$; **, $P < 0.01$; Mann–Whitney test. Scale bars, 10 µm (A–D).

2005; Basak et al., 2015; Duregotti et al., 2015). To investigate Nrg1 type III function during axon remodeling, we crossed floxed Nrg1 type III (Velanac et al., 2012) to TdTomato reporter mice and injected neonates with AAV9-*CMV*-iCre (Fig. S3 E). As expected, myelination was severely impaired in TdTomato-positive branches compared with internal control axons (Fig. S3, F–H). We further tested if increased Nrg1 type III levels are sufficient to remove the competition-dependent block on myelination using *Thy1*-Nrg1 type III-HA mice, where Nrg1 type III is tagged with hemagglutinin (Fig. 6, A and B). Here, axon remodeling was transiently accelerated (Lee et al., 2016), and overall nodes form significantly earlier (Fig. 6, C–F; Velanac et al., 2012). Notably the myelination delay on competing din branches was preserved, most likely reflecting the distribution of Nrg1 type III (Fig. 6 F).

To analyze local distribution of Nrg1 type III with single-axon precision, we immunostained for the HA-tag and visualized SCs and axons (Fig. 7, A and B). We detected a higher HA signal along winner sin branches compared with competing din axons, in line with differential trafficking regulated by competition-regulated cytoskeletal maturation (Fig. 7 C). Corroborating differential Nrg1 signaling, we measured significantly higher levels of activated forms of both ERK1/2 (pERK) and AKT (pAKT) surrounding winner sin axons (Fig. 7, D–G). As myelination initiation on winner branches was reduced following neurotransmission blockade, HA-tagged Nrg1 type III and pERK signals also significantly decreased in sin branches (Fig. 7, H and I). Transgenic expression of Nrg1 type III did not change the density or area of AChRs (Fig. 7, J and K). Therefore, Nrg1 type III

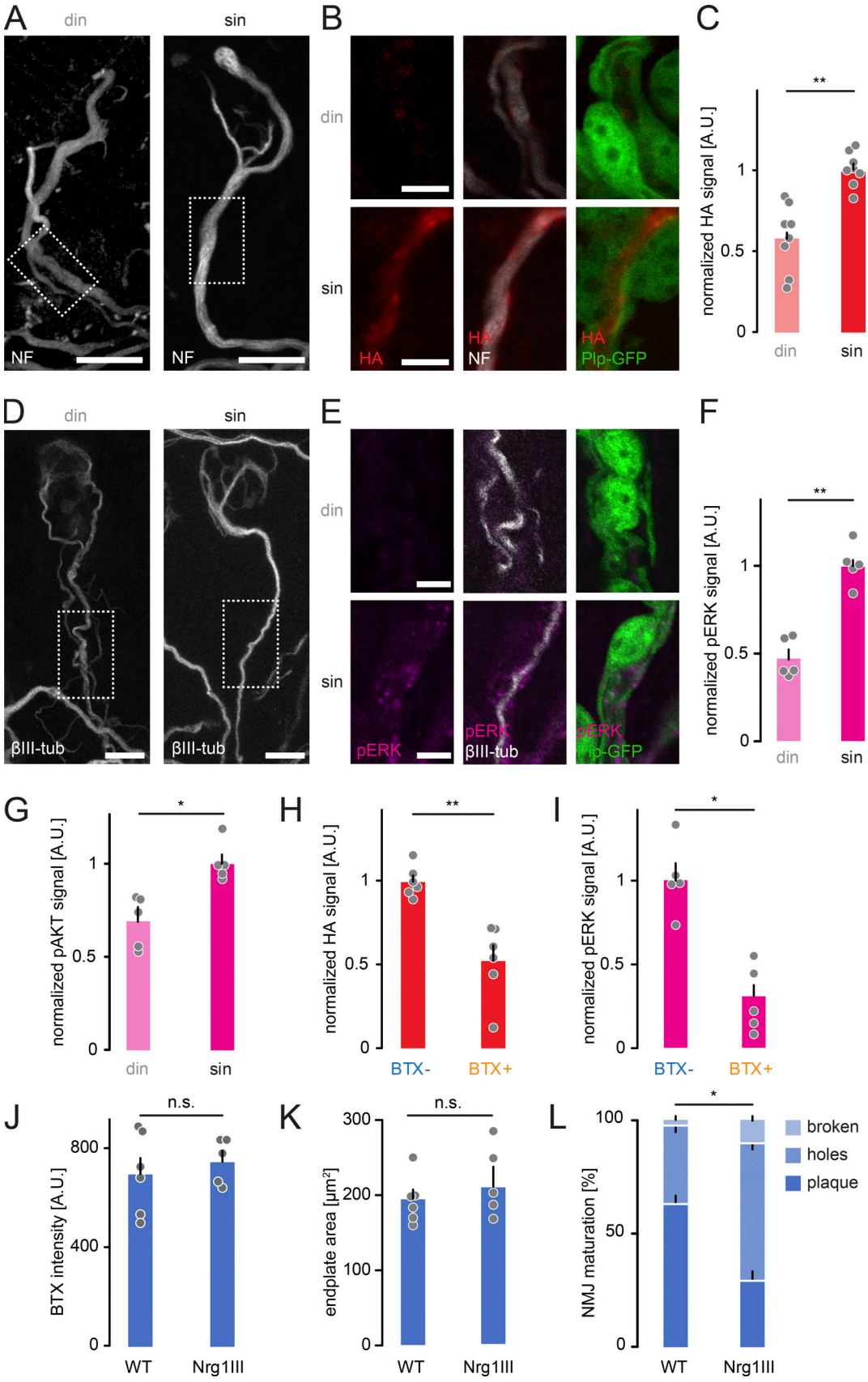

Figure 7. **Nrg1 type III is more concentrated on singly innervating terminal branches. (A and B)** *Plp*-GFP × *Thy1*-Nrg1 type III-HA mouse immunostained for neurofilament (NF; white) in P9 triangularis sterni muscle. A projected overview of competing (din) versus winner branches (sin); dashed boxes enlarged in

B show magnified single optical sections of HA staining (red) with GFP-labeled SCs (green). **(C)** Quantification of HA staining on doubly versus singly innervating branches in *Thy1*-Nrg1 type III animals (n = 8 mice per genotype, ≥13 axons per animal). **(D and E)** *Plp*-GFP × *Thy1*-Nrg1 type III-HA mice immunostained for βIII-tubulin (white) in P9 triangularis sterni muscle. A projected overview (D) of competing (din) versus winner branches (sin); dashed boxes enlarged in E show magnified single optical sections of pERK staining (magenta) with GFP-labeled SCs (green). **(F)** Quantification of pERK staining around doubly versus singly innervating branches in *Thy1*-Nrg1 type III animals (n = 5 mice per genotype, ≥20 axons per animal). **(G)** Quantification of pAKT immunostaining around doubly versus singly innervating branches in *Thy1*-Nrg1 type III animals, normalized to singly innervating branches (≥20 axons per group in n = 5 mice). **(H)** Quantification of HA signal in singly innervating axons in BTX-injected triangularis sterni muscle versus uninjected control side (≥13 axons per group in n = 6 mice). **(I)** Quantification of pERK signal in SCs surrounding singly innervating axons in BTX-injected triangularis sterni muscle versus uninjected control side (≥36 axons per group in n = 5 mice). **(J)** BTX intensity measured in WT and *Thy1*-Nrg1 type III transgenic animals (WT, 698 ± 67 arbitrary units [A.U.], *Thy1*-Nrg1 type III, 747 ± 43 A.U.; n ≥ 16 NMJ per animal, n ≥ 5 mice per group). **(K)** Area of BTX-stained endplate measured in WT and *Thy1*-Nrg1 type III transgenic animals (WT, 195 ± 13 μm^2; *Thy1*-Nrg1 type III, 203 ± 22 μm^2; n ≥ 16 NMJ per animal, n ≥ 5 mice per group). **(L)** Quantification of the proportions of NMJ morphology, categorized into "broken," "holes," and "plaque" (n ≥ 5 mice per group, ≥14 NMJ per animal). din, competing axons; sin, winner axons. Data represent mean + SEM. *, P < 0.05; **, P < 0.01; Mann–Whitney test. Scale bars represent 10 µm (A and D) and 5 µm (B and E).

likely impacts myelination via its promyelinating effects rather than by modulating postsynaptic feedback (Velanac et al., 2012; Kamezaki et al., 2016). Indeed, the only phenotype we observed at the endplate was a premature shape change of the AChR distribution in *Thy1*-Nrg1 type III-HA mice compared with WT littermates (Fig. 7 L; Lee et al., 2016).

Discussion

Taken together, our data suggest that during motor axon remodeling, a promyelination signal (such as Nrg1) paces branch myelination, which is limited by axonal transport and depends on local regulation of cytoskeletal integrity. Thus, axon–glial differentiation is delayed until competition resolves and the axonal cytoskeleton matures. Notably, according to this model, axon dismantling and myelination initiation both depend on mechanisms that regulate the microtubular cytoskeleton (Brill et al., 2016). This model also links anterograde transport to a signaling function, which previously was mostly considered for retrograde transport, such as delivering neurotrophic factors (Je et al., 2012; Yamashita, 2019).

The intersection of axon remodeling and myelination is widespread (Feinberg, 1982; Bernstein and Lichtman, 1999; Woo and Crowell, 2005; Barres, 2008) and might play a general role in the activity-dependent sculpting of efficient neuronal networks (Luo and O'Leary, 2005; Tapia and Lichtman, 2012; de Hoz and Simons, 2015; Chang et al., 2016). The prevailing notion has been that myelination might terminate axonal plasticity by "cementing" axons in place, thus contributing to closing the critical remodeling period (Caroni and Schwab, 1988; McGee et al., 2005; Geoffroy and Zheng, 2014; Kalish et al., 2020). Indeed, we observed myelination initiation predominantly on winner axon branches (sin), i.e., after competition was resolved (Fig. 1). However, while determining the exact start and progression speed of myelination is technically challenging (thus, we resorted to a "binary" readout of Caspr-positive vs. Caspr-negative branches), our observations clearly reveal that competition delayed myelination, but not vice versa (Fig. 3). A subset of competing axons still initiated myelination, but this did not convey a measurable advantage during competition, as no relationship between myelination and synaptic territory was apparent in our data. Even some retreating axons were myelinated, including in cases where the likely competing branch was not (Fig. 3 G). Still, in general, myelination was prevented on axon branches that were fated for removal. As myelin is an extremely stable structure (Simons and Trotter, 2007; Hughes et al., 2018), which might be metabolically "expensive" to build (Nave and Trapp, 2008; Harris and Attwell, 2012) and requires a dedicated mechanism for dismantling, it seems economical to delay myelination until pruning is resolved (McGee et al., 2005; Cheng and Carr, 2007). Thus, our results support a view where myelin might act as participant in, but not as the terminator of circuit plasticity (Mount and Monje, 2017).

How do competing axon branches delay myelination? A number of cell biological features of such branches scale with its synaptic territory during competition, including cytoskeletal stability, organelle transport, or axon caliber (Keller-Peck et al., 2001; Brill et al., 2016). We can rule out the hypothesis that axon caliber dictates myelination onset, since axon caliber did not differ between myelinated and unmyelinated competing branches (Fig. 3 D; Goebbels et al., 2010), even though we found evidence that along a given branch, myelination has an impact on local diameter (Fig. 3 E). To further probe the mechanism that times myelination onset, we manipulated activity-driven competition (Buffelli et al., 2003) using local BTX injections (Fig. 4). This intervention is muscle specific and therefore less likely to affect axon–SC communication compared with blocking axonal action potential conduction or acetylcholine release (Misgeld et al., 2002; Lorenzetto et al., 2009). Notably, while there exists some cholinergic axon–SC communication, this typically involves BTX-insensitive receptors (Rousse and Robitaille, 2006). In the past, chronic blockade of neuromuscular transmission, such as in chicken embryos treated with curare, has been shown to result in AChR cluster fragmentation and axonal sprouting (cf. Loeb et al., 2002; Loeb, 2003). Also, constitutive genetic ablation of choline acetyl transferase in motor axons leads to premature myelination in the phrenic nerve at birth (Misgeld et al., 2002). Still, these outcomes likely reflect the combination of presynaptic and sustained blockade, prone to elicit homeostatic compensation (Davis, 2013). Here, by using brief and local postsynaptic blockade, we found the expected delay in axon remodeling but also a commensurate hiatus in myelination (Fig. 4, D and E). Thus, myelination onset appears to be part of the BTX-sensitive competition program, revealing an indirect role of neurotransmission in regulating the progress of PNS myelination (for the CNS, cf. Stevens et al., 2002; Gibson et al., 2014; Krasnow et al., 2018). Moreover, postsynaptic block induced a reduction in presynaptic microtubular mass on

winner branches (Fig. 4, F and G), suggesting a silencing-induced delay in maturation, which chimes with a cytoskeletal mechanism of inducing myelination.

Indeed, in terminal axon branches, the microtubular cytoskeleton matures in parallel to an increase in synaptic territory (Brill et al., 2016). Accordingly, we observed that spastin deletion, which increased microtubular mass (Fig. 4, L and M), resulted in accelerated myelination specifically on competing branches, breaking the link between remodeling and myelination delay (Fig. 4 K). However, spastin deletion in winner branches did not affect the initiation of myelination. This suggests that the limiting factor in this setting could be cargo instead of track availability, as we reported previously for mitochondria (Marahori, 2020). Microtubular content can locally regulate axonal transport (Kapitein and Hoogenraad, 2015; Roll-Mecak, 2019), hinting that myelination might depend on branch-specific transport. To test this, we expressed a dominant-negative kinesin mutant in vivo, which affects anterograde organelle delivery (Cai et al., 2005; Barry et al., 2014). In both zebrafish and mouse motor neurons, this delayed myelination, despite the transport blockade being partial and short (Fig. 5 and Fig. S4). Taken together, our data suggest that in competing branches, transport of promyelinating cargos is restricted by an immature and increasingly severed microtubular cytoskeleton (Brill et al., 2016).

Since our FRAP experiments suggest that nodal components are not limited in competing branches (Fig. 2; but cf. Roche et al., 2014), we focused on Nrg1 type III as the putative factor determining myelination onset for the following reasons: Nrg1 signaling (1) is the master regulator of PNS myelination (Birchmeier and Nave, 2008; Grigoryan and Birchmeier, 2015); (2) acts in a threshold-based manner (Garratt et al., 2000; Michailov et al., 2004; Taveggia et al., 2005; Nave and Salzer, 2006); and (3) is steeply up-regulated during the synapse remodeling period (Lee et al., 2016), while its axonal presence is limited (Velanac et al., 2012). Indeed, we demonstrated that HA-tagged Nrg1 accumulates faster on winner than on competing branches (Fig. 7 C), and that downstream pathways of Nrg1 signaling are preferentially activated in SCs around winner branches (Fig. 7, F and G). It would have further strengthened our argument if increased Nrg1 could be observed in spastin-deleted axons. Likely due to chromosomal incompatibility of the Nrg1 transgene insertion site and the spastin locus, we failed in showing this, but instead tested the converse setting and showed that HA-tagged Nrg1 distribution and downstream signaling decrease upon BTX blockade (Fig. 7, H and I). The fact that Nrg1 overexpression accelerates both myelination and synapse elimination (Fig. 6; Lee et al., 2016) further strengthens our conclusion that myelination per se does not terminate remodeling. However, it is technically challenging to disambiguate whether Nrg1 signals directly from the axonal surface to myelinating SCs or through a more complicated feedback via muscle and/or terminal SCs. Yet we did not measure a difference in postsynaptic AChR density or area between *Thy1*-Nrg1 type III-HA and WT littermates (Fig. 7), suggesting Nrg1 likely functions via its promyelinating effects rather than by modulating muscular depolarization.

In summary, our experiments reveal an intercellular signaling mechanism that regulates myelination on a branch-to-branch level in the developing PNS. The extent of branch-specific Nrg1 accumulation, and hence the strength of the promyelination signal, are regulated by the axonal cytoskeleton as a spatially resolved signaling hub (Janke, 2014). A similar local regulation between neuronal remodeling and myelination can be relevant in many developing neural circuits, as certain cortical axon types are myelinated in a highly local fashion (Tomassy et al., 2014; Micheva et al., 2016). Moreover, when disturbed, such signaling could contribute to the disrupted timing of developmental events characteristic of some neuropsychiatric disorders, where axonal transport, neuronal remodeling, and myelination all show subtle defects (Coleman and Perry, 2002; Luo and O'Leary, 2005; Mei and Nave, 2014).

Materials and methods

Mouse lines and husbandry

In all experiments, mice from both sexes were included. Animals were housed in individually ventilated cages with food and water ad libitum. All animal experiments were performed in accordance with the regulations by the local authorities (e.g., Government of Upper Bavaria). Experimental animals were kept together with littermates.

Experimental mice and genotyping

For labeling axons, we used *Thy1*-XFP mice, which express OFP (*Thy1*-OFP3; Brill et al., 2011), YFP (*Thy1*-YFP16; Feng et al., 2000), or membrane-RFP (*Thy1*-Brainbow-1.1 line M; Livet et al., 2007) under control of the *Thy1*-promotor (Feng et al., 2000). For FRAP experiments and node visualization in living explants, we used *Thy1*-Caspr-GFP (Brivio et al., 2017) and *Thy1*-β1-Nav-GFP transgenic mice (generated for this study; see below) crossed to *Thy1*-XFP mice. Synaptic territory of competing axonal branches was defined in *Thy1*-Brainbow-1.1 line M mice crossed to Cre-expressing lines: *CAG*-CreERT (gift from Dr. J. Livet, Institut de la Vision, Paris, France) or *ChAT*-IRES-Cre (Jackson; #6410; Rossi et al., 2011), which leads to individual fluorescent color combinations of membrane-targeted RFP, YFP, and CFP. For the crossing involving *CAG*-CreERT, 20 µl of 1.5 mg/ml tamoxifen was subcutaneously injected on P3 to induce expression. Delayed synapse elimination was analyzed in spastin knockout (KO) mice (Brill et al., 2016) or spastin floxed ($^{fl/fl}$) mice bred to *ROSA-CAG*-TdTomato or YFP reporter mice (Jackson; #7914, #7903; Madisen et al., 2010) injected with AAV9-CMV-iCre (Brill et al., 2016). Effects of transport modulation on myelin and nodal development was observed in TdTomato reporter mice crossed to *Thy1*-β1-Nav-GFP or *ROSA-CAG*-YFP mice injected with AAV9-hSyn-iCre-p2a-KHC-CBD. Precocious myelination was investigated in *Thy1*-Nrg1 type III-HA mice ("HANI"; Velanac et al., 2012). To investigate delayed nodal development, we injected AAV9-CMV-iCre into conditional Neuregulin KO mice (Nrg1 type III$^{fl/fl}$; Velanac et al., 2012) crossbred with *ROSA-CAG*-TdTomato reporter. To visualize SCs, we used *Plp*-GFP transgenic mice (Mallon et al., 2002). All

experiments on *ROSA-CAG*-TdTomato or -YFP reporter mice were performed in homozygous animals.

Genomic DNA was extracted from tail biopsies using a one-step lysis (lysis buffer in mM: 67 Tris, pH 8.8, 16.6 $(NH_4)_2SO_4$, 6.5 $MgCl_2$, 5 β-mercaptoethanol, 10% Triton, and 50 µg/ml Proteinase K; incubation at 55°C for 5 h, followed by inactivation step 5 min at 95°C). PCR was performed with GoTaq Green Master Mix (Promega; #M7121) following a standard protocol, and then DNA was separated on a 1.5–2% agarose gel. Genotyping primers and expected products are listed in Table S1.

Generation of Thy1-β1-Nav-GFP transgenic mice

Transgenic mice expressing the β1 subunit of the sodium channel (β1-Nav) fused to GFP at the C-terminus under control of the *Thy1.2* promoter (Caroni, 1997) were generated by pronuclear injection. β1-Nav-GFP cDNA (McEwen et al., 2009) was cloned into the blunted XhoI site of the pTSC21k vector (Lüthi et al., 1997), released using Not I (Zonta et al., 2011), and used for pronuclear injection (Sherman and Brophy, 2000).

FRAP experiments and Caspr-GFP trafficking in nerve-muscle explant

Nerve-muscle explants from the thorax, including the triangularis sterni muscle, were prepared from young (P7–P14) or adult mice (6 wk; Kerschensteiner et al., 2008; Brill et al., 2011, 2016). The rib cage was isolated from euthanized animals, and the skin and pectoral muscles over the rib cage were removed. The diaphragm was cut and the thorax was released by cutting the ribs close to the vertebral column. The dissection was continued in oxygenated precooled Ringer's solution (in mM: 125 NaCl, 2.5 KCl, 1.25 NaH_2PO_4, 26 $NaHCO_3$, 2 $CaCl_2$, 1 $MgCl_2$, and 20 glucose, oxygenated with 95% O_2/5% CO_2) in a 10-cm dish, and remnants of muscles, thymus, pleura, and lung were removed. The clean nerve-muscle explant was pinned onto a Sylgard-coated 3.5-cm dish, superfused with oxygenated Ringer's solution, using shortened insect pins (Fine Science Tools; 26001–25, 0.25 mm), exposing the triangularis sterni muscle, the intercostal nerve, and terminal motor neuron branches. During imaging, the explant was kept at 31–33°C with a heating ring connected to an automatic temperature controller (Warner Instruments; TC-344C) and steadily perfused with Ringer's solution.

Trafficking measurements of β1-Nav-GFP particles in the terminal branches were performed with an Olympus BX51WI epifluorescence microscope equipped with ×20/0.5 NA and ×100/1.0 NA water-immersion objectives, an automated filter wheel (Sutter Instruments; Lambda 10–3), a charge-coupled device camera (Visitron Systems; CoolSnap HQ2), and a GFP ET filter set (AHF Analysentechnik). All devices were controlled by µManager 1.4 (Edelstein et al., 2014). Per movie, we acquired 200 images at 1 Hz using an exposure time of 500 ms. Total imaging time on explants was restricted to maximum 2 h, except for FRAP analysis (below).

For FRAP analysis, we used *Thy1*-Caspr-GFP and *Thy1*-β1-Nav-GFP mice and the same setup as described above for transport measurements. The laser (Rapp OptoElectronic; 473 nm, DL-473) for photobleaching was manually focused on a labeled node of Ranvier (~5 µm²), and the sample was bleached for 1–3 s. We performed FRAP on branches with heminodes during development, since fully developed nodes are rare at the investigated age. In adults, all measurements were performed on fully developed nodes. The GFP signal was imaged with 800-ms exposure time before and immediately after photobleaching with a GFP/mCherry dualband ET filter set (AHF Analysentechnik) and then in 1-h intervals for 3 h again with 800-ms exposure time.

Mouse immunofluorescence and confocal microscopy

The thorax was fixed in 4% PFA for 1 h in 0.1 M phosphate buffer (PB) on ice and the triangularis muscle was dissected and extracted (Brill et al., 2011). For HA staining, the sample was additionally treated for 1 h at 37°C in 5% CHAPS. The fixed thorax was incubated overnight (or 72 h for HA, pERK, and pAKT) at 4°C in the respective primary antibodies diluted in blocking solution (5% BSA and 0.5% Triton X-100 in 0.1 M PB). To label postsynaptic nicotinic AChRs, Alexa Fluor 488, Alexa Fluor 594, Alexa Fluor 647, or biotin conjugated to BTX (Invitrogen, B13422, B13423, B35450, B1196; 50 µg/ml, 1:50) was added to the primary antibody mixture. The following primary antibodies were used in this study: anti-βIII-tubulin conjugated to Alexa Fluor 488 (BioLegend; AB_2562669; mouse IgG2a, 1:200), Alexa Fluor 555 (BD PharMingen; #560339; mouse monoclonal, 1:200), and Alexa Fluor 647 (BioLegend; AB_2563609; mouse IgG2a, 1:200). For labeling of nodal components antibodies against Caspr (Abcam; AB_869934, polyclonal rabbit; 1 mg/ml 1:400), MPZ (Aves Labs; combined chicken IgY, 200 µg/ml, 1:200), CNTN2 (R&D Systems; AB_2044647; polyclonal goat IgG, 1:200), and pan Nav subunit α (Abgent; AG1392; polyclonal rabbit, 1.0 mg/ml, 1:400). HA was stained with anti–HA-tag antibody (Cell Signaling; AB_1549585; rabbit, 1:50), and phosphorylated ERK1/2 was stained with anti-phospho-p44/42 MAPK (Cell Signaling; AB_331646; rabbit, 1:200), while pAKT was stained with anti–phospho-Akt (Cell Signaling; AB_329824; rabbit, 1:200). Here, we used tyramide signal amplification (PerkinElmer; TSA Cyanine 3 System, AB_2572409). Muscles were washed in 0.1 M PB, incubated for 1 h at room temperature with corresponding secondary antibodies coupled to Alexa Fluor 488, Alexa Fluor 594, or Alexa Fluor 647 (Invitrogen; rabbit: #A-11070, #A-11072, #A-21246, #A-32790; mouse: #A-11005; chicken: #A-11042; #A-21449; goat: #A-11058) and washed again in 0.1 M PB. Muscles were mounted in Vectashield (Vector Laboratories) or Fluoromont-G (Southern Biotech), and image stacks were recorded using a confocal microscope (Olympus; FV1000) equipped with ×20/0.8 NA and ×60/1.42 NA oil-immersion objectives (Olympus).

Generation of recombinant DNA

To generate the pTREK1-*hSyn*-iCre-p2a-KHC-CBD construct for the AAV9-*hSyn*-iCre-p2a-KHC-CBD production, we used the Gibson Assembly Master Mix (NEB). We recombined fragments from pEGFP-C1-KHC-CBD (Cai et al., 2005), the dsCMV-iCre and pAAV-*hSyn*-DIO-HA-hM3D(Gq)-IRES-mCitrine plasmid (Addgene; #50454), and the p2a sequence. The produced amplicon was ligated into the single-stranded AAV backbone plasmid pTREK1. The following oligonucleotides were used: 5′-AGTACTTAATACGACTCACTATAGGAT

GGTGCCCAAGAAG-3′, 5′-TCCACGTCGCCGGCCTGCTTCAGC AGGGAGAAGTTGGTGGCGTCCCCATCCTCGA-3′, 5′-TGCTGA AGCAGGCCGGCGACGTGGAGGAGAACCCCGGCCCCAGTG CTGAGATTGATTCT-3′, and 5′-ATCATGTCTGGATCCTCGATA GTTTAAACTTACACTTGTTTGCCTC-3′.

For zebrafish injections, we generated pDestTol2CG2_UAS: GFP-KHC-CBD-polyA and pTol2_cntn1b:KHC-CBD-GFP vectors using the Gateway system (Thermo Fisher Scientific). To produce the middle entry clone pME_GFP-KHC-CBD, the GFP-KHC-CBD sequence was amplified from the template plasmid (Cai et al., 2005). The PCR product was then recombined into the vector pDONR221 using BP clonase (Thermo Fisher Scientific). The final expression constructs pTol2_UAS:GFP-KHC-CBD and pTol2_cntn1b:GFP-KHC-CBD were then generated in multisite LR recombination reactions (Thermo Fisher Scientific) with the entry clones, p5E_UAS, p5E_cntn1b, pME_GFP-KHC-CBD, p3E_pA, and pDestTol2_pA of the Tol2Kit (Kwan et al., 2007).

Generation of AAV9

HEK293-T cells were grown in 10-tray Cell Factories (Thermo Fisher Scientific) using Dulbecco's modified essential medium (Gibco) with 10% fetal bovine serum (Gibco) and 1% penicillin/streptomycin (Gibco). The cells were split into the Cell Factories 24 h before transfection to reach 80% confluence at the time of transfection. Then, 420 µg of the pTREK1-*hSyn*-iCre-p2a-KHC-CBD plasmid and 1.5 mg of the helper plasmid (pDP9rs, kindly provided by Roger Hajjar, Phospholamban Foundation, Amsterdam, Netherlands) were introduced into the HEK293-T cells using polyethyleneimine (Polysciences). 3 d later, the cells were harvested, lysed, and benzonase treated, and the virus was isolated by ultracentrifugation through an iodixanol density gradient (Progen; OptiPrep). Ringer lactate buffer (Braun) was used to replace iodixanol with the help of Vivaspin 20 columns and molecuar weight cut-off 100,000 polyethersulfone membrane (Sartorius). Two 10-tray Cell Factories were pooled and concentrated to a total volume of 500 µl. AAV9 titers were determined by real-time PCR using SYBR Green Master Mix (Roche). Titers in the range of 10^{14} viral genome copies per milliliter were acquired.

Neonatal AAV9 or BTX injection

AAV9 was injected into neonatal pups according to previously published protocol (Passini and Wolfe, 2001). In short, P3 pups were anaesthetized with isoflurane (Abbott) and injected with 3 µl AAV9-CMV-iCre or AAV9-hSyn-iCre-p2A-KHC particles into the right lateral ventricle at a rate of 30 nl/s using a fine glass pipette (Drummond; 3.5", #3-000-203-G/X) attached to a nanoliter injector (World Precision Instruments; Micro4 MicroSyringe Pump Controller connected with Nanoliter 2000). All surgeries were conducted under ultrasound guidance (Visualsonics; Vevo1100 Imaging System, with a Microscan MS550D transducer). 0.05% (wt/vol) trypan blue was added to the viral solution for visualizing the filling of the injected ventricles. Only whole litters were injected, and pups were allowed to recover on a heating mat before the litter was returned to their mother into the home cage and sacrificed on P9 for immunohistochemistry. To monitor Cre-mediated recombination, mice carried in addition to the respective genes (spastin or Nrg1 type III conditional KO) two TdTomato or YFP reporter alleles (homozygous), which resulted in robust expression of the reporter in a subset of motor neurons.

Injection of BTX on P7 was administered in a similar manner, but the needle was inserted laterally under the skin of the right thorax, and 1 µl of a 50 mg/µl Alexa Fluor 488– or Alexa Fluor 594–conjugated BTX solution (Invitrogen; B13422, B13423) was injected. The contralateral (left) triangularis sterni muscle was unaffected and used as control. The injected pups were viable and active after the treatment and not distinguishable from untreated controls. Ipsi- and contralateral triangularis sterni muscles were then post hoc stained with Alexa Fluor 594– or Alexa Fluor 488–conjugated BTX, respectively, resulting in complementing stainings for blocked and unblocked AChRs. We confirmed a substantial degree of persisting blockade at P9 (11.9 ± 4.5 fold change of BTX staining on injected vs. noninjected side, $n \geq 50$ NMJs in five mice) and the absence of denervation (>100 NMJs per mouse, $n = 3$ mice).

Zebrafish injection, immunostaining, and confocal imaging

Fertilized Tg(mbp:RFP)^{tum102Tg} eggs (Auer et al., 2018) at the one-cell stage were pressure microinjected with 1 nl solution containing 20–40 ng/µl plasmid DNA (*cntn1b*:GFP-KHC-CBD or control *cntn1b:GFP*; Auer et al., 2018) and 25–50 ng/µl transposase mRNA. For immunohistochemistry, larval zebrafish at 6 dpf were euthanized with 4 mg/ml MS-222 (PHARMAQ) and then fixed overnight in 4% PFA in 0.1 M PB. After fixation, the samples were washed three times in PBS and 0.1% Tween20, immersed for 2 h at room temperature in blocking solution (5% BSA and 0.5% Triton X-100 in 0.1 M PB), and then incubated in primary antibody against α-tubulin (Sigma-Aldrich; #00020911, mouse, 1:200) at 4°C for 48 h in blocking solution. Samples were washed and incubated in secondary antibody conjugated to Alexa Fluor 647 (Invitrogen; goat-anti-mouse #A-28181) overnight at 4°C (Hunter et al., 2011). Samples were washed again and embedded in Vectashield (Vector Laboratories). Image stacks were recorded using a confocal microscope (Olympus; FV1000) equipped with a ×20/0.8 NA oil-immersion objective.

To label Rohon–Beard neurons, fertilized embryos from WT fish were coinjected with a sensory neuron–specific Gal4 driver construct (containing enhancer elements from *isl1*; Sagasti et al., 2005) together with UAS:KHC-CBD-GFP and UAS:mitoTagRFP-T plasmids (each at 5 ng/ul). Alternatively, UAS:KHC-CBD-GFP and UAS:mitoTagRFP-T plasmids were coinjected into fertilized eggs from the *isl2b*:Gal4 line (Ben Fredj et al., 2010). At 2 dpf, embryos were anesthetized using 0.2 mg/ml MS-222 (PHARMAQ) and embedded in UltraPure Low Melting Point Agarose (Thermo Fisher Scientific) on a glass coverslip. After selecting double-labeled Rohon–Beard neurons, mitochondrial transport was imaged for at least 50 min in the stem axon using the wide-field microscope configured as in the FRAP experiments. We acquired movies with an imaging frequency of 2 Hz and an exposure time between 200 and 500 ms for each fish (Plucińska et al., 2012).

Image processing/representation and quantification

Innervation patterns were determined by counting the number of innervating terminal branches ending on each BTX-stained NMJ in ImageJ/Fiji (Schindelin et al., 2012). The myelination status of a terminal branch (axon from last bifurcation until NMJ) was determined by any presence of clustered markers of nodal or internodal differentiation (Caspr, CNTN2, MPZ, and Nav). Immunostaining on branchpoints was excluded due to difficulties to discern from the more prominent nodal structures on the stem axon. Axon diameter was determined by measuring the area of the entire terminal branch divided by the length of the branch, resulting in an averaged axon diameter. We verified the precision of our axonal diameter measurement by comparison with other methods to determine axonal diameter (e.g., averaged multisite measurements and determination of smallest diameter) and found no significant difference between Caspr-positive and Caspr-negative axons in measured caliber with the different approaches we tested.

Tubulin content of axons was determined by manually placing regions of interest in a single optical section within an axon, and the mean gray values were averaged for each channel. We have previously established that immunohistochemically determined tubulin content correlates linearly with microtubule density as measured by electron microscopy, once corrected for an offset likely representing nonpolymerized tubulin (Brill et al., 2016).

For FRAP analysis, in-focus images were manually aligned, and the intensity of the bleached area was measured with the polygon tool. The background intensity was measured in a dark and even area, and another GFP-positive paranode in the same field of view was used as control to correct for the recovery rate.

For zebrafish myelination, the motor axon length was determined using the segmented line tool based on α-tubulin staining, and the length of the myelinated stretch was likewise determined based on mbp:RFP fluorescence.

Colocalization of GFP-positive Nav puncta and antibody staining was analyzed in single optical sections of unprocessed images.

To determine transport rates of mitochondria or β1-Nav-GFP particles traveling along the axons, we counted the number of fluorescent particles passing through a region in focus of the axon quantified.

For image representation, maximum intensity projections were generated from confocal image stacks with ImageJ/Fiji and then further processed in Adobe Photoshop, where channels were adjusted individually. For better visibility of dim structures, gamma was adjusted in images that only represent morphological detail; no gamma adjustment was performed in quantitative images (all panels in Fig. 2, A and C; Fig. 4, F and L; Fig. 6, A and B; Fig. 7, B and E; and Fig. S2 G).

All analyses were performed with the experimenter blinded to the treatment or genotypes during imaging and scoring.

Statistical analysis

Statistical tests were performed using GraphPad Prism software. Statistical significance was determined using the Mann–Whitney test (nonparametric test for two groups), following the Kruskal–Wallis test with post hoc Dunn's multiple comparisons test (nonparametric test for three or more groups), respectively. An unpaired *t* test was used when the dataset passed the D'Agostino and Pearson normality test. The χ^2 test was used for comparing expected frequencies between groups, and the P value calculated from the test was shown. Group sizes were determined using experience values from prior studies (e.g., Brill et al., 2016; Plucińska et al., 2012). $P < 0.05$ was considered to be significant (*, $P < 0.05$; **, $P < 0.01$; ***, $P < 0.001$; ****, $P < 0.0001$). Bar graphs show mean + SEM. Violin plots depict median and quartiles excluding the outliers, which were identified with Tukey's test (Fig. 2, B and D; Fig. 5, B; Fig. S2, H; and Fig. S3 D).

Online supplemental material

Fig. S1 shows characterization of Thy1-Caspr-GFP and Thy1-β1-Nav-GFP mice. Fig. S2 shows that innervation and myelination status correlate with axonal tubulin content and SC length. Fig. S3 shows that AAV9-mediated spastin deletion promotes myelination on competing branches. Fig. S4 shows that microtubule-dependent axonal transport affects myelination onset. Table S1 lists the mouse lines and genotyping primers used.

Acknowledgments

We would like to thank M. and N. Budak, K. Wullimann, and Y. Hufnagel for excellent technical assistance. We thank Dr. L. Godinho for critically reading the manuscript. We are grateful to Dr. J. Livet (Institut de la Vision, Paris, France) for the generous gift of *CAG*-CreERT mice and Dr. J. Trimmer (University of California, Davis, Davis, CA) for the Caspr antibody.

Work in T. Misgeld's laboratory is supported by the Deutsche Forschungsgemeinschaft (CIPSM EXC114, CRC870, FOR 2879, Mi 694/7-1, 8-1, and 9-1-428663564, TRR274 - TRR 274/1 2020; ID 408885537, projects B03, C02), the European Research Council (FP/2007-2013; ERC grant agreement 616791), the Gemeinnützige Hertie Stiftung, the German-Israeli Foundation for Scientific Research and Development (I-1200-237.1/2012), the Elite Network Bavaria (S-LW-2016-351), the German Center for Neurodegenerative Diseases, and Technische Universität München's Institute for Advanced Studies. T. Misgeld and M.S. Brill were further funded by the Deutsche Forschungsgemeinschaft–funded Excellence Cluster SyNergy (EXC 2145 – ID 390857198). M.S. Brill is recipient of a Deutsche Forschungsgemeinschaft research grant (LE 4610/1-1; 450131873). M. Wang received support from the Technische Universität München PhD program Medical Life Sciences and Technology. D.L. Sherman and P.J. Brophy were supported by the Wellcome Trust (grant 107008).

The authors declare no competing financial interests.

Author contributions: Conceptualization, M. Wang, T. Misgeld, and M.S. Brill; investigation, M. Wang, T. Kleele, G. Plucinska, and Y. Xiao; methodology, D.L. Sherman and P.J. Brophy; resources, P. Avramopoulos, S. Engelhardt, M.H. Schwab, P.J. Brophy, D.L. Sherman, M. Kneussel, and T. Czopka; writing – original draft, M. Wang, T. Misgeld, and M.S. Brill; writing – review and editing, all authors; supervision, T. Misgeld and M.S. Brill; funding acquisition, T. Misgeld.

Submitted: 5 December 2019
Revised: 20 November 2020
Accepted: 4 January 2021

References

Akaaboune, M., S.M. Culican, S.G. Turney, and J.W. Lichtman. 1999. Rapid and reversible effects of activity on acetylcholine receptor density at the neuromuscular junction in vivo. *Science.* 286:503–507. https://doi.org/10.1126/science.286.5439.503

Auer, F., S. Vagionitis, and T. Czopka. 2018. Evidence for myelin sheath remodeling in the CNS revealed by in vivo imaging. *Curr. Biol.* 28: 549–559.e3. https://doi.org/10.1016/j.cub.2018.01.017

Bacmeister, C.M., H.J. Barr, C.R. McClain, M.A. Thornton, D. Nettles, C.G. Welle, and E.G. Hughes. 2020. Motor learning promotes remyelination via new and surviving oligodendrocytes. *Nat. Neurosci.* 23:819–831. https://doi.org/10.1038/s41593-020-0637-3

Barres, B.A. 2008. The mystery and magic of glia: a perspective on their roles in health and disease. *Neuron.* 60:430–440. https://doi.org/10.1016/j.neuron.2008.10.013

Barry, J., Y. Gu, P. Jukkola, B. O'Neill, H. Gu, P.J. Mohler, K.T. Rajamani, and C. Gu. 2014. Ankyrin-G directly binds to kinesin-1 to transport voltage-gated Na+ channels into axons. *Dev. Cell.* 28:117–131. https://doi.org/10.1016/j.devcel.2013.11.023

Basak, S., D.J. Desai, E.H. Rho, R. Ramos, P. Maurel, and H.A. Kim. 2015. E-cadherin enhances neuregulin signaling and promotes Schwann cell myelination. *Glia.* 63:1522–1536. https://doi.org/10.1002/glia.22822

Ben Fredj, N., S. Hammond, H. Otsuna, C.B. Chien, J. Burrone, and M.P. Meyer. 2010. Synaptic activity and activity-dependent competition regulates axon arbor maturation, growth arrest, and territory in the retinotectal projection. *J. Neurosci.* 30:10939–10951. https://doi.org/10.1523/JNEUROSCI.1556-10.2010

Bernstein, M., and J.W. Lichtman. 1999. Axonal atrophy: the retraction reaction. *Curr. Opin. Neurobiol.* 9:364–370. https://doi.org/10.1016/S0959-4388(99)80053-1

Birchmeier, C., and K.A. Nave. 2008. Neuregulin-1, a key axonal signal that drives Schwann cell growth and differentiation. *Glia.* 56:1491–1497. https://doi.org/10.1002/glia.20753

Bishop, D.L., T. Misgeld, M.K. Walsh, W.B. Gan, and J.W. Lichtman. 2004. Axon branch removal at developing synapses by axosome shedding. *Neuron.* 44:651–661. https://doi.org/10.1016/j.neuron.2004.10.026

Brill, M.S., J.W. Lichtman, W. Thompson, Y. Zuo, and T. Misgeld. 2011. Spatial constraints dictate glial territories at murine neuromuscular junctions. *J. Cell Biol.* 195:293–305. https://doi.org/10.1083/jcb.201108005

Brill, M.S., P. Marinković, and T. Misgeld. 2013. Sequential photo-bleaching to delineate single Schwann cells at the neuromuscular junction. *J. Vis. Exp.* 71:e4460. https://doi.org/10.3791/4460

Brill, M.S., T. Kleele, L. Ruschkies, M. Wang, N.A. Marahori, M.S. Reuter, T.J. Hausrat, E. Weigand, M. Fisher, A. Ahles, et al. 2016. Branch-specific microtubule destabilization mediates axon branch loss during neuromuscular synapse elimination. *Neuron.* 92:845–856. https://doi.org/10.1016/j.neuron.2016.09.049

Brivio, V., C. Faivre-Sarrailh, E. Peles, D.L. Sherman, and P.J. Brophy. 2017. Assembly of CNS nodes of Ranvier in myelinated nerves is promoted by the axon cytoskeleton. *Curr. Biol.* 27:1068–1073. https://doi.org/10.1016/j.cub.2017.01.025

Buffelli, M., R.W. Burgess, G. Feng, C.G. Lobe, J.W. Lichtman, and J.R. Sanes. 2003. Genetic evidence that relative synaptic efficacy biases the outcome of synaptic competition. *Nature.* 424:430–434. https://doi.org/10.1038/nature01844

Cai, Q., C. Gerwin, and Z.H. Sheng. 2005. Syntabulin-mediated anterograde transport of mitochondria along neuronal processes. *J. Cell Biol.* 170: 959–969. https://doi.org/10.1083/jcb.200506042

Caroni, P. 1997. Overexpression of growth-associated proteins in the neurons of adult transgenic mice. *J. Neurosci. Methods.* 71:3–9. https://doi.org/10.1016/S0165-0270(96)00121-5

Caroni, P., and M.E. Schwab. 1988. Antibody against myelin-associated inhibitor of neurite growth neutralizes nonpermissive substrate properties of CNS white matter. *Neuron.* 1:85–96. https://doi.org/10.1016/0896-6273(88)90212-7

Chang, K.-J., S.A. Redmond, and J.R. Chan. 2016. Remodeling myelination: implications for mechanisms of neural plasticity. *Nat. Neurosci.* 19: 190–197. https://doi.org/10.1038/nn.4200

Cheng, S.M., and C.E. Carr. 2007. Functional delay of myelination of auditory delay lines in the nucleus laminaris of the barn owl. *Dev. Neurobiol.* 67: 1957–1974. https://doi.org/10.1002/dneu.20541

Coleman, M.P., and V.H. Perry. 2002. Axon pathology in neurological disease: a neglected therapeutic target. *Trends Neurosci.* 25:532–537. https://doi.org/10.1016/S0166-2236(02)02255-5

Czopka, T., and D.A. Lyons. 2011. Dissecting mechanisms of myelinated axon formation using zebrafish. Methods Cell Biol. 105:25–62.

D'Rozario, M., K.R. Monk, and S.C. Petersen. 2017. Analysis of myelinated axon formation in zebrafish. *Methods Cell Biol.* 138:383–414. https://doi.org/10.1016/bs.mcb.2016.08.001

Davis, G.W. 2013. Homeostatic signaling and the stabilization of neural function. *Neuron.* 80:718–728. https://doi.org/10.1016/j.neuron.2013.09.044

de Hoz, L., and M. Simons. 2015. The emerging functions of oligodendrocytes in regulating neuronal network behaviour. *BioEssays.* 37:60–69. https://doi.org/10.1002/bies.201400127

Doyle, J.P., and D.R. Colman. 1993. Glial-neuron interactions and the regulation of myelin formation. *Curr. Opin. Cell Biol.* 5:779–785. https://doi.org/10.1016/0955-0674(93)90025-L

Duregotti, E., S. Negro, M. Scorzeto, I. Zornetta, B.C. Dickinson, C.J. Chang, C. Montecucco, and M. Rigoni. 2015. Mitochondrial alarmins released by degenerating motor axon terminals activate perisynaptic Schwann cells. *Proc. Natl. Acad. Sci. USA.* 112:E497–E505. https://doi.org/10.1073/pnas.1417108112

Edelstein, A.D., M.A. Tsuchida, N. Amodaj, H. Pinkard, R.D. Vale, and N. Stuurman. 2014. Advanced methods of microscope control using μManager software. *J. Biol. Methods.* 1:10. https://doi.org/10.14440/jbm.2014.36

Etxeberria, A., K.C. Hokanson, D.Q. Dao, S.R. Mayoral, F. Mei, S.A. Redmond, E.M. Ullian, and J.R. Chan. 2016. Dynamic modulation of myelination in response to visual stimuli alters optic nerve conduction velocity. *J. Neurosci.* 36:6937–6948. https://doi.org/10.1523/JNEUROSCI.0908-16.2016

Feinberg, I. 1982. Schizophrenia: caused by a fault in programmed synaptic elimination during adolescence? *J. Psychiatr. Res.* 17:319–334. https://doi.org/10.1016/0022-3956(82)90038-3

Feng, G., R.H. Mellor, M. Bernstein, C. Keller-Peck, Q.T. Nguyen, M. Wallace, J.M. Nerbonne, J.W. Lichtman, and J.R. Sanes. 2000. Imaging neuronal subsets in transgenic mice expressing multiple spectral variants of GFP. *Neuron.* 28:41–51. https://doi.org/10.1016/S0896-6273(00)00084-2

Fields, R.D. 2015. A new mechanism of nervous system plasticity: activity-dependent myelination. *Nat. Rev. Neurosci.* 16:756–767. https://doi.org/10.1038/nrn4023

Gan, W.B., and J.W. Lichtman. 1998. Synaptic segregation at the developing neuromuscular junction. *Science.* 282:1508–1511. https://doi.org/10.1126/science.282.5393.1508

Garratt, A.N., O. Voiculescu, P. Topilko, P. Charnay, and C. Birchmeier. 2000. A dual role of erbB2 in myelination and in expansion of the schwann cell precursor pool. *J. Cell Biol.* 148:1035–1046. https://doi.org/10.1083/jcb.148.5.1035

Geoffroy, C.G., and B. Zheng. 2014. Myelin-associated inhibitors in axonal growth after CNS injury. *Curr. Opin. Neurobiol.* 27:31–38. https://doi.org/10.1016/j.conb.2014.02.012

Gibson, E.M., D. Purger, C.W. Mount, A.K. Goldstein, G.L. Lin, L.S. Wood, I. Inema, S.E. Miller, G. Bieri, J.B. Zuchero, et al. 2014. Neuronal activity promotes oligodendrogenesis and adaptive myelination in the mammalian brain. *Science.* 344:1252304. https://doi.org/10.1126/science.1252304

Girault, J.A., and E. Peles. 2002. Development of nodes of Ranvier. *Curr. Opin. Neurobiol.* 12:476–485. https://doi.org/10.1016/S0959-4388(02)00370-7

Goebbels, S., J.H. Oltrogge, R. Kemper, I. Heilmann, I. Bormuth, S. Wolfer, S.P. Wichert, W. Möbius, X. Liu, C. Lappe-Siefke, et al. 2010. Elevated phosphatidylinositol 3,4,5-trisphosphate in glia triggers cell-autonomous membrane wrapping and myelination. *J. Neurosci.* 30:8953–8964. https://doi.org/10.1523/JNEUROSCI.0219-10.2010

Grigoryan, T., and W. Birchmeier. 2015. Molecular signaling mechanisms of axon-glia communication in the peripheral nervous system. *BioEssays.* 37:502–513. https://doi.org/10.1002/bies.201400172

Harris, J.J., and D. Attwell. 2012. The energetics of CNS white matter. *J. Neurosci.* 32:356–371. https://doi.org/10.1523/JNEUROSCI.3430-11.2012

Hayworth, C.R., S.E. Moody, L.A. Chodosh, P. Krieg, M. Rimer, and W.J. Thompson. 2006. Induction of neuregulin signaling in mouse schwann

cells in vivo mimics responses to denervation. *J. Neurosci.* 26:6873–6884. https://doi.org/10.1523/JNEUROSCI.1086-06.2006

Hildebrand, C., C.M. Bowe, and I.N. Remahl. 1994. Myelination and myelin sheath remodelling in normal and pathological PNS nerve fibres. *Prog. Neurobiol.* 43:85–141. https://doi.org/10.1016/0301-0082(94)90010-8

Hirokawa, N., Y. Noda, Y. Tanaka, and S. Niwa. 2009. Kinesin superfamily motor proteins and intracellular transport. *Nat. Rev. Mol. Cell Biol.* 10: 682–696. https://doi.org/10.1038/nrm2774

Huff, T.B., Y. Shi, W. Sun, W. Wu, R. Shi, and J.X. Cheng. 2011. Real-time CARS imaging reveals a calpain-dependent pathway for paranodal myelin retraction during high-frequency stimulation. *PLoS One.* 6: e17176. https://doi.org/10.1371/journal.pone.0017176

Hughes, E.G., J.L. Orthmann-Murphy, A.J. Langseth, and D.E. Bergles. 2018. Myelin remodeling through experience-dependent oligodendrogenesis in the adult somatosensory cortex. *Nat. Neurosci.* 21:696–706. https://doi.org/10.1038/s41593-018-0121-5

Hunter, P.R., N. Nikolaou, B. Odermatt, P.R. Williams, U. Drescher, and M.P. Meyer. 2011. Localization of Cadm2a and Cadm3 proteins during development of the zebrafish nervous system. *J. Comp. Neurol.* 519: 2252–2270. https://doi.org/10.1002/cne.22627

Huxley, A.F., and R. Stämpeli. 1949. Evidence for saltatory conduction in peripheral myelinated nerve fibres. *J. Physiol.* 108:315–339. https://doi.org/10.1113/jphysiol.1949.sp004335

Iwakura, Y., and H. Nawa. 2013. ErbB1-4-dependent EGF/neuregulin signals and their cross talk in the central nervous system: pathological implications in schizophrenia and Parkinson's disease. *Front. Cell. Neurosci.* 7:4. https://doi.org/10.3389/fncel.2013.00004

Janke, C. 2014. The tubulin code: molecular components, readout mechanisms, and functions. *J. Cell Biol.* 206:461–472. https://doi.org/10.1083/jcb.201406055

Je, H.S., F. Yang, Y. Ji, G. Nagappan, B.L. Hempstead, and B. Lu. 2012. Role of pro-brain-derived neurotrophic factor (proBDNF) to mature BDNF conversion in activity-dependent competition at developing neuromuscular synapses. *Proc. Natl. Acad. Sci. USA.* 109:15924–15929. https://doi.org/10.1073/pnas.1207767109

Jessen, K.R., and R. Mirsky. 2005. The origin and development of glial cells in peripheral nerves. *Nat. Rev. Neurosci.* 6:671–682. https://doi.org/10.1038/nrn1746

Kalish, B.T., T.R. Barkat, E.E. Diel, E.J. Zhang, M.E. Greenberg, and T.K. Hensch. 2020. Single-nucleus RNA sequencing of mouse auditory cortex reveals critical period triggers and brakes. *Proc. Natl. Acad. Sci. USA.* 117:11744–11752. https://doi.org/10.1073/pnas.1920433117

Kaller, M.S., A. Lazari, C. Blanco-Duque, C. Sampaio-Baptista, and H. Johansen-Berg. 2017. Myelin plasticity and behaviour-connecting the dots. *Curr. Opin. Neurobiol.* 47:86–92. https://doi.org/10.1016/j.conb.2017.09.014

Kamezaki, A., F. Sato, K. Aoki, K. Asakawa, K. Kawakami, F. Matsuzaki, and A. Sehara-Fujisawa. 2016. Visualization of Neuregulin 1 ectodomain shedding reveals its local processing in vitro and in vivo. *Sci. Rep.* 6: 28873. https://doi.org/10.1038/srep28873

Kano, M., and K. Hashimoto. 2009. Synapse elimination in the central nervous system. *Curr. Opin. Neurobiol.* 19:154–161. https://doi.org/10.1016/j.conb.2009.05.002

Kapitein, L.C., and C.C. Hoogenraad. 2015. Building the Neuronal Microtubule Cytoskeleton. *Neuron.* 87:492–506. https://doi.org/10.1016/j.neuron.2015.05.046

Keller-Peck, C.R., M.K. Walsh, W.B. Gan, G. Feng, J.R. Sanes, and J.W. Lichtman. 2001. Asynchronous synapse elimination in neonatal motor units: studies using GFP transgenic mice. *Neuron.* 31:381–394. https://doi.org/10.1016/S0896-6273(01)00383-X

Kerschensteiner, M., M.S. Reuter, J.W. Lichtman, and T. Misgeld. 2008. Ex vivo imaging of motor axon dynamics in murine triangularis sterni explants. *Nat. Protoc.* 3:1645–1653. https://doi.org/10.1038/nprot.2008.160

Korrell, K.V., J. Disser, K. Parley, A. Vadisiute, M.C. Requena-Komuro, H. Fodder, C. Pollart, G. Knott, Z. Molnár, and A. Hoerder-Suabedissen. 2019. Differential effect on myelination through abolition of activity-dependent synaptic vesicle release or reduction of overall electrical activity of selected cortical projections in the mouse. *J. Anat.* 235: 452–467. https://doi.org/10.1111/joa.12974

Krasnow, A.M., M.C. Ford, L.E. Valdivia, S.W. Wilson, and D. Attwell. 2018. Regulation of developing myelin sheath elongation by oligodendrocyte calcium transients in vivo. *Nat. Neurosci.* 21:24–28. https://doi.org/10.1038/s41593-017-0031-y

Kummer, T.T., T. Misgeld, J.W. Lichtman, and J.R. Sanes. 2004. Nerve-independent formation of a topologically complex postsynaptic apparatus. *J. Cell Biol.* 164:1077–1087. https://doi.org/10.1083/jcb.200401115

Kwan, K.M., E. Fujimoto, C. Grabher, B.D. Mangum, M.E. Hardy, D.S. Campbell, J.M. Parant, H.J. Yost, J.P. Kanki, and C.B. Chien. 2007. The Tol2kit: a multisite gateway-based construction kit for Tol2 transposon transgenesis constructs. *Dev. Dyn.* 236:3088–3099. https://doi.org/10.1002/dvdy.21343

Lee, Y.I., Y. Li, M. Mikesh, I. Smith, K.-A. Nave, M.H. Schwab, and W.J. Thompson. 2016. Neuregulin1 displayed on motor axons regulates terminal Schwann cell-mediated synapse elimination at developing neuromuscular junctions. *Proc. Natl. Acad. Sci. USA.* 113:E479–E487. https://doi.org/10.1073/pnas.1519156113

Lichtman, J.W., and J.R. Sanes. 2003. Watching the neuromuscular junction. *J. Neurocytol.* 32:767–775. https://doi.org/10.1023/B:NEUR.0000020622.58471.37

Livet, J., T.A. Weissman, H. Kang, R.W. Draft, J. Lu, R.A. Bennis, J.R. Sanes, and J.W. Lichtman. 2007. Transgenic strategies for combinatorial expression of fluorescent proteins in the nervous system. *Nature.* 450: 56–62. https://doi.org/10.1038/nature06293

Loeb, J.A. 2003. Neuregulin: an activity-dependent synaptic modulator at the neuromuscular junction. *J. Neurocytol.* 32:649–664. https://doi.org/10.1023/B:NEUR.0000020640.84708.35

Loeb, J.A., A. Hmadcha, G.D. Fischbach, S.J. Land, and V.L. Zakarian. 2002. Neuregulin expression at neuromuscular synapses is modulated by synaptic activity and neurotrophic factors. *J. Neurosci.* 22:2206–2214. https://doi.org/10.1523/JNEUROSCI.22-06-02206.2002

Lorenzetto, E., L. Caselli, G. Feng, W. Yuan, J.M. Nerbonne, J.R. Sanes, and M. Buffelli. 2009. Genetic perturbation of postsynaptic activity regulates synapse elimination in developing cerebellum. *Proc. Natl. Acad. Sci. USA.* 106:16475–16480. https://doi.org/10.1073/pnas.0907298106

Luo, L., and D.D.M. O'Leary. 2005. Axon retraction and degeneration in development and disease. *Annu. Rev. Neurosci.* 28:127–156. https://doi.org/10.1146/annurev.neuro.28.061604.135632

Lüthi, A., H. Van der Putten, F.M. Botteri, I.M. Mansuy, M. Meins, U. Frey, G. Sansig, C. Portet, M. Schmutz, M. Schröder, et al. 1997. Endogenous serine protease inhibitor modulates epileptic activity and hippocampal long-term potentiation. *J. Neurosci.* 17:4688–4699. https://doi.org/10.1523/JNEUROSCI.17-12-04688.1997

Madisen, L., T.A. Zwingman, S.M. Sunkin, S.W. Oh, H.A. Zariwala, H. Gu, L.L. Ng, R.D. Palmiter, M.J. Hawrylycz, A.R. Jones, et al. 2010. A robust and high-throughput Cre reporting and characterization system for the whole mouse brain. *Nat. Neurosci.* 13:133–140. https://doi.org/10.1038/nn.2467

Mallon, B.S., H.E. Shick, G.J. Kidd, and W.B. Macklin. 2002. Proteolipid promoter activity distinguishes two populations of NG2-positive cells throughout neonatal cortical development. *J. Neurosci.* 22:876–885. https://doi.org/10.1523/JNEUROSCI.22-03-00876.2002

Marahori, N.A. 2020. Cytoskeletal Rearrangement during Developmental Motor Axon Remodeling. Technical University Munich, Munich, Germany. 98 pp.

McEwen, D.P., C. Chen, L.S. Meadows, L. Lopez-Santiago, and L.L. Isom. 2009. The voltage-gated Na+ channel β3 subunit does not mediate trans homophilic cell adhesion or associate with the cell adhesion molecule contactin. *Neurosci. Lett.* 462:272–275. https://doi.org/10.1016/j.neulet.2009.07.020

McGee, A.W., Y. Yang, Q.S. Fischer, N.W. Daw, and S.M. Strittmatter. 2005. Experience-driven plasticity of visual cortex limited by myelin and Nogo receptor. *Science.* 309:2222–2226. https://doi.org/10.1126/science.1114362

Mei, L., and K.A. Nave. 2014. Neuregulin-ERBB signaling in the nervous system and neuropsychiatric diseases. *Neuron.* 83:27–49. https://doi.org/10.1016/j.neuron.2014.06.007

Mensch, S., M. Baraban, R. Almeida, T. Czopka, J. Ausborn, A. El Manira, and D.A. Lyons. 2015. Synaptic vesicle release regulates myelin sheath number of individual oligodendrocytes in vivo. *Nat. Neurosci.* 18: 628–630. https://doi.org/10.1038/nn.3991

Michailov, G.V., M.W. Sereda, B.G. Brinkmann, T.M.H. Fischer, B. Haug, C. Birchmeier, L. Role, C. Lai, M.H. Schwab, and K.-A.A. Nave. 2004. Axonal neuregulin-1 regulates myelin sheath thickness. *Science.* 304: 700–703. https://doi.org/10.1126/science.1095862

Micheva, K.D., D. Wolman, B.D. Mensh, E. Pax, J. Buchanan, S.J. Smith, and D.D. Bock. 2016. A large fraction of neocortical myelin ensheathes axons of local inhibitory neurons. *eLife.* 5:e15784. https://doi.org/10.7554/eLife.15784

Misgeld, T., R.W. Burgess, R.M. Lewis, J.M. Cunningham, J.W. Lichtman, and J.R. Sanes. 2002. Roles of neurotransmitter in synapse formation: development of neuromuscular junctions lacking choline acetyltransferase. *Neuron.* 36:635–648. https://doi.org/10.1016/S0896-6273(02)01020-6

Monk, K.R., M.L. Feltri, and C. Taveggia. 2015. New insights on Schwann cell development. *Glia.* 63:1376–1393. https://doi.org/10.1002/glia.22852

Mount, C.W., and M. Monje. 2017. Wrapped to Adapt: Experience-Dependent Myelination. *Neuron.* 95:743–756. https://doi.org/10.1016/j.neuron.2017.07.009

Nave, K.A. 2010. Myelination and support of axonal integrity by glia. *Nature.* 468:244–252. https://doi.org/10.1038/nature09614

Nave, K.A., and J.L. Salzer. 2006. Axonal regulation of myelination by neuregulin 1. *Curr. Opin. Neurobiol.* 16:492–500. https://doi.org/10.1016/j.conb.2006.08.008

Nave, K.-A., and B.D. Trapp. 2008. Axon-glial signaling and the glial support of axon function. *Annu. Rev. Neurosci.* 31:535–561. https://doi.org/10.1146/annurev.neuro.30.051606.094309

Ogata, T., S. Iijima, S. Hoshikawa, T. Miura, S. Yamamoto, H. Oda, K. Nakamura, and S. Tanaka. 2004. Opposing extracellular signal-regulated kinase and Akt pathways control Schwann cell myelination. *J. Neurosci.* 24:6724–6732. https://doi.org/10.1523/JNEUROSCI.5520-03.2004

Passini, M.A., and J.H. Wolfe. 2001. Widespread gene delivery and structure-specific patterns of expression in the brain after intraventricular injections of neonatal mice with an adeno-associated virus vector. *J. Virol.* 75:12382–12392. https://doi.org/10.1128/JVI.75.24.12382-12392.2001

Pereira, J.A., F. Lebrun-Julien, and U. Suter. 2012. Molecular mechanisms regulating myelination in the peripheral nervous system. *Trends Neurosci.* 35:123–134. https://doi.org/10.1016/j.tins.2011.11.006

Peters, A., S.L. Palay, and H.D.F. Webster. 1991. The Neurones and Supporting Cells, in the Fine Structure of the Nervous System. Oxford University Press, New York. 496 pp.

Plucińska, G., D. Paquet, A. Hruscha, L. Godinho, C. Haass, B. Schmid, and T. Misgeld. 2012. In vivo imaging of disease-related mitochondrial dynamics in a vertebrate model system. *J. Neurosci.* 32:16203–16212. https://doi.org/10.1523/JNEUROSCI.1327-12.2012

Rasband, M.N., and E. Peles. 2015. The nodes of Ranvier: Molecular assembly and maintenance. *Cold Spring Harb. Perspect. Biol.* 8:a020495. https://doi.org/10.1101/cshperspect.a020495

Rios, J.C., C.V. Melendez-Vasquez, S. Einheber, M. Lustig, M. Grumet, J. Hemperly, E. Peles, and J.L. Salzer. 2000. Contactin-associated protein (Caspr) and contactin form a complex that is targeted to the paranodal junctions during myelination. *J. Neurosci.* 20:8354–8364. https://doi.org/10.1523/JNEUROSCI.20-22-08354.2000

Roche, S.L., D.L. Sherman, K. Dissanayake, G. Soucy, A. Desmazieres, D.J. Lamont, E. Peles, J.-P. Julien, T.M. Wishart, R.R. Ribchester, et al. 2014. Loss of glial neurofascin155 delays developmental synapse elimination at the neuromuscular junction. *J. Neurosci.* 34:12904–12918. https://doi.org/10.1523/JNEUROSCI.1725-14.2014

Roll-Mecak, A. 2019. How cells exploit tubulin diversity to build functional cellular microtubule mosaics. *Curr. Opin. Cell Biol.* 56:102–108. https://doi.org/10.1016/j.ceb.2018.10.009

Rossi, J., N. Balthasar, D. Olson, M. Scott, E. Berglund, C.E. Lee, M.J. Choi, D. Lauzon, B.B. Lowell, and J.K. Elmquist. 2011. Melanocortin-4 receptors expressed by cholinergic neurons regulate energy balance and glucose homeostasis. *Cell Metab.* 13:195–204. https://doi.org/10.1016/j.cmet.2011.01.010

Rousse, I., and R. Robitaille. 2006. Calcium signaling in Schwann cells at synaptic and extra-synaptic sites: active glial modulation of neuronal activity. *Glia.* 54:691–699. https://doi.org/10.1002/glia.20388

Sagasti, A., M.R. Guido, D.W. Raible, and A.F. Schier. 2005. Repulsive interactions shape the morphologies and functional arrangement of zebrafish peripheral sensory arbors. *Curr. Biol.* 15:804–814. https://doi.org/10.1016/j.cub.2005.03.048

Schafer, D.P., A.W. Custer, P. Shrager, and M.N. Rasband. 2006. Early events in node of Ranvier formation during myelination and remyelination in the PNS. *Neuron Glia Biol.* 2:69–79. https://doi.org/10.1017/S1740925X06000093

Schindelin, J., I. Arganda-Carreras, E. Frise, V. Kaynig, M. Longair, T. Pietzsch, S. Preibisch, C. Rueden, S. Saalfeld, B. Schmid, et al. 2012. Fiji: an open-source platform for biological-image analysis. *Nat. Methods.* 9:676–682. https://doi.org/10.1038/nmeth.2019

Sherman, D.L., and P.J. Brophy. 2000. A tripartite nuclear localization signal in the PDZ-domain protein L-periaxin. *J. Biol. Chem.* 275:4537–4540. https://doi.org/10.1074/jbc.275.7.4537

Simons, M., and J. Trotter. 2007. Wrapping it up: the cell biology of myelination. *Curr. Opin. Neurobiol.* 17:533–540. https://doi.org/10.1016/j.conb.2007.08.003

Stevens, B., and R.D. Fields. 2000. Response of Schwann cells to action potentials in development. *Science.* 287:2267–2271. https://doi.org/10.1126/science.287.5461.2267

Stevens, B., S. Porta, L.L. Haak, V. Gallo, and R.D. Fields. 2002. Adenosine: a neuron-glial transmitter promoting myelination in the CNS in response to action potentials. *Neuron.* 36:855–868. https://doi.org/10.1016/S0896-6273(02)01067-X

Tapia, J.C., and J.W. Lichtman. 2012. Synapse Elimination. *In* Fundamental Neuroscience: Fourth Edition. 437–455.

Tapia, J.C., J.D. Wylie, N. Kasthuri, K.J. Hayworth, R. Schalek, D.R. Berger, C. Guatimosim, H.S. Seung, and J.W. Lichtman. 2012. Pervasive synaptic branch removal in the mammalian neuromuscular system at birth. *Neuron.* 74:816–829. https://doi.org/10.1016/j.neuron.2012.04.017

Taveggia, C., G. Zanazzi, A. Petrylak, H. Yano, J. Rosenbluth, S. Einheber, X. Xu, R.M. Esper, J.A. Loeb, P. Shrager, et al. 2005. Neuregulin-1 type III determines the ensheathment fate of axons. *Neuron.* 47:681–694. https://doi.org/10.1016/j.neuron.2005.08.017

Taveggia, C., M.L. Feltri, and L. Wrabetz. 2010. Signals to promote myelin formation and repair. *Nat. Rev. Neurol.* 6:276–287. https://doi.org/10.1038/nrneurol.2010.37

Tomassy, G.S., D.R. Berger, H.H. Chen, N. Kasthuri, K.J. Hayworth, A. Vercelli, H.S. Seung, J.W. Lichtman, and P. Arlotta. 2014. Distinct profiles of myelin distribution along single axons of pyramidal neurons in the neocortex. *Science.* 344:319–324. https://doi.org/10.1126/science.1249766

Turney, S.G., and J.W. Lichtman. 2012. Reversing the outcome of synapse elimination at developing neuromuscular junctions in vivo: evidence for synaptic competition and its mechanism. *PLoS Biol.* 10:e1001352. https://doi.org/10.1371/journal.pbio.1001352

Vabnick, I., and P. Shrager. 1998. Ion channel redistribution and function during development of the myelinated axon. *J. Neurobiol.* 37:80–96. https://doi.org/10.1002/(SICI)1097-4695(199810)37:1<80::AID-NEU7>3.0.CO;2-4

Velanac, V., T. Unterbarnscheidt, W. Hinrichs, M.N. Gummert, T.M. Fischer, M.J. Rossner, A. Trimarco, V. Brivio, C. Taveggia, M. Willem, et al. 2012. Bace1 processing of NRG1 type III produces a myelin-inducing signal but is not essential for the stimulation of myelination. *Glia.* 60:203–217. https://doi.org/10.1002/glia.21255

Voyvodic, J.T. 1989. Target size regulates calibre and myelination of sympathetic axons. *Nature.* 342:430–433. https://doi.org/10.1038/342430a0

Walsh, M.K., and J.W. Lichtman. 2003. In vivo time-lapse imaging of synaptic takeover associated with naturally occurring synapse elimination. *Neuron.* 37:67–73. https://doi.org/10.1016/S0896-6273(02)01142-X

Woo, T.U.W., and A.L. Crowell. 2005. Targeting synapses and myelin in the prevention of schizophrenia. *Schizophr. Res.* 73:193–207. https://doi.org/10.1016/j.schres.2004.07.022

Yamamoto, K., A.C. Merry, and A.A.F. Sima. 1996. An orderly development of paranodal axoglial junctions and bracelets of Nageotte in the rat sural nerve. *Brain Res. Dev. Brain Res.* 96:36–45. https://doi.org/10.1016/0165-3806(96)00072-7

Yamashita, N. 2019. Retrograde signaling via axonal transport through signaling endosomes. *J. Pharmacol. Sci.* 141:91–96. https://doi.org/10.1016/j.jphs.2019.10.001

Yin, X., R.C. Baek, D.A. Kirschner, A. Peterson, Y. Fujii, K.A. Nave, W.B. Macklin, and B.D. Trapp. 2006. Evolution of a neuroprotective function of central nervous system myelin. *J. Cell Biol.* 172:469–478. https://doi.org/10.1083/jcb.200509174

Zhang, Y., Y. Bekku, Y. Dzhashiashvili, S. Armenti, X. Meng, Y. Sasaki, J. Milbrandt, and J.L. Salzer. 2012. Assembly and maintenance of nodes of ranvier rely on distinct sources of proteins and targeting mechanisms. *Neuron.* 73:92–107. https://doi.org/10.1016/j.neuron.2011.10.016

Zonta, B., A. Desmazieres, A. Rinaldi, S. Tait, D.L. Sherman, M.F. Nolan, and P.J. Brophy. 2011. A critical role for Neurofascin in regulating action potential initiation through maintenance of the axon initial segment. *Neuron.* 69:945–956. https://doi.org/10.1016/j.neuron.2011.02.021

Supplemental material

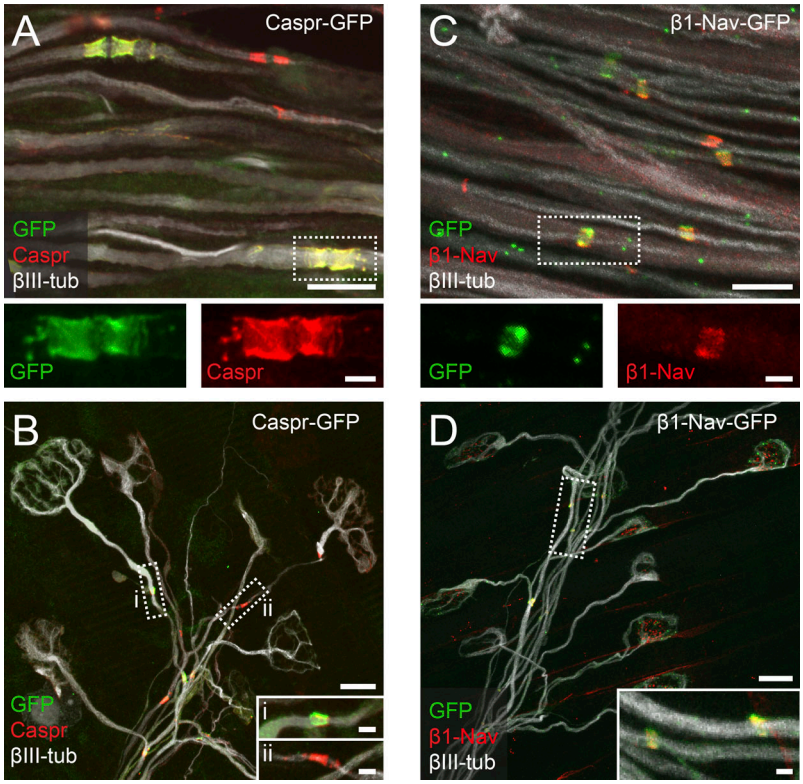

Figure S1. **Characterization of *Thy1*-Caspr-GFP and *Thy1*-β1-Nav-GFP mice. (A)** Confocal image of P9 *Thy1*-Caspr-GFP (native GFP, green) intercostal axons (βIII-tubulin, white) immunostained for Caspr (red). Dashed boxes enlarged below show single channels. The percentage of GFP-positive paranodes nodes was stable across development, suggesting consistent labeling of a neuronal subset (P9–P11: 65 ± 8% of all paranodal structures; 6 wk: 73 ± 9%; P = 0.7, Mann–Whitney test; *n* = 4 mice per age group, ≥44 nodes per animal). **(B)** Triangularis sterni muscle of a P9 *Thy1*-Caspr-GFP mouse immunostained for Caspr (red) and axons (βIII-tubulin, white). Dashed boxes enlarged below show Caspr/GFP double-positive (i) and Caspr-only–positive paranodes (ii). Expression of the Caspr-GFP transgene did not detectably influence the degree of double innervation (WT, 9 ± 1% vs. Caspr-GFP, 12 ± 2%; P = 0.4, Mann–Whitney test; *n* = 3 mice per genotype, ≥136 axons per animal) or myelination on terminal axon branches at P9 (winner branches: WT, 32 ± 2% vs. Caspr-GFP, 35 ± 8%; competing branches: WT, 12 ± 6% vs. Caspr-GFP, 7 ± 7%; P > 0.99, Mann–Whitney test; *n* = 3 mice per genotype, ≥31 axons per animal). **(C)** Image of P9 *Thy1*-β1-Nav-GFP (native GFP, green) intercostal axons (βIII-tubulin, white) immunostained for Nav (red). Dashed boxes enlarged below show single channels. All nodes identified by immunostaining were also GFP positive, indicating transgene expression in all motor neurons (100 ± 0%; *n* = 3 mice, ≥40 axons per animal). **(D)** Triangularis sterni muscle of a P9 *Thy1*-β1-Nav-GFP mouse immunostained for Nav (red) along terminal axon branches (βIII-tubulin, white). Insets show enlarged Nav/GFP double-positive nodes. Expression of the β1-Nav-GFP transgene did not detectably influence the degree of double innervation (WT, 11 ± 1% vs. β1-Nav-GFP, 14 ± 2%; *n* = 3 mice per genotype, ≥102 axons; P = 0.7, Mann–Whitney test; axons per animal) or myelination on terminal axon branches at P9 (winner branches: WT, 38 ± 8% vs. β1-Nav-GFP, 30 ± 4%; competing branches: WT, 19 ± 3% vs. β1-Nav-GFP, 11 ± 6%; P > 0.4, Mann–Whitney test; *n* = 3 mice per genotype, ≥31 axons per animal). din, competing axons; sin, winner axons. Scale bars represent 10 µm (A–D, overview) and 2 µm (insets).

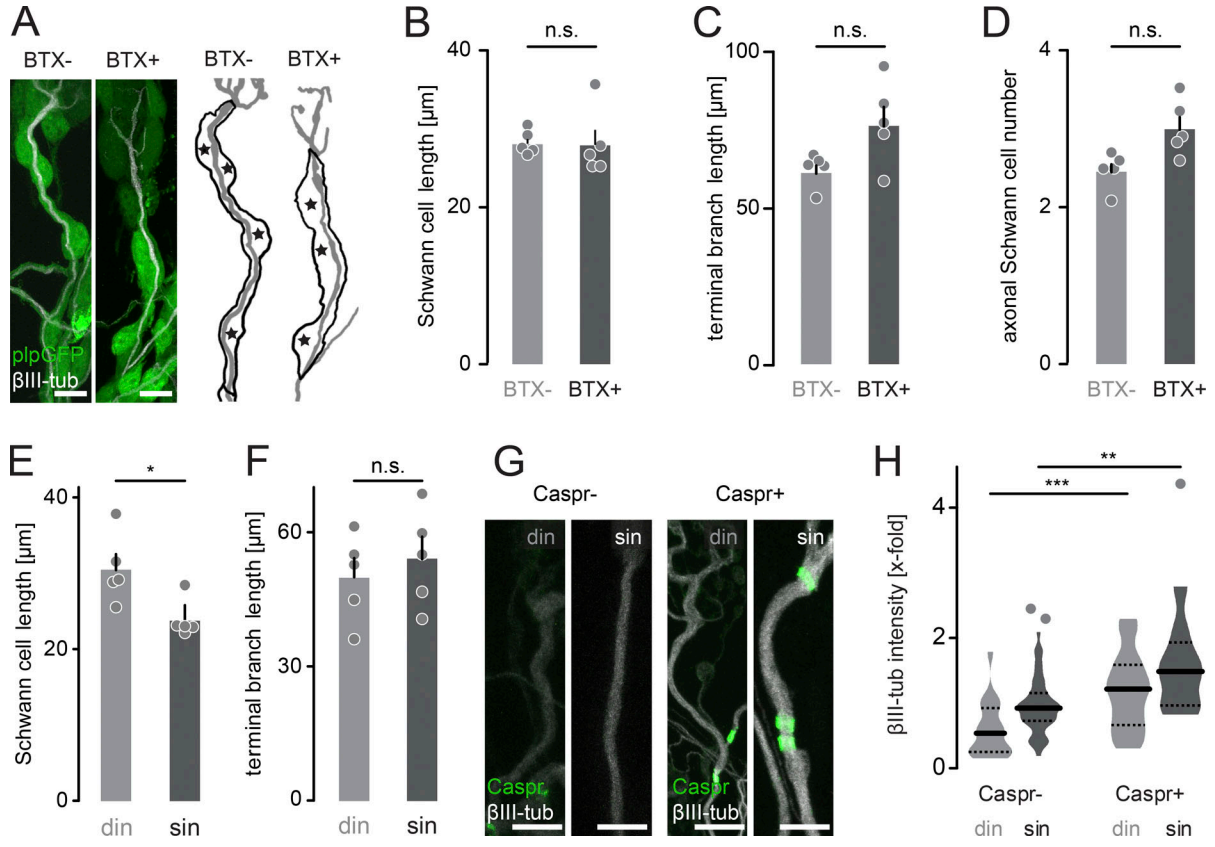

Figure S2. **Innervation and myelination status correlate with axonal tubulin content and SC length. (A)** Images of SCs on singly innervating terminal branches in a *Plp*-GFP (green) mouse following BTX injection on P7 versus contralateral control side and post hoc staining at P9 with βIII-tubulin (white). Schematics to the right depict measured terminal axon length (gray) and SC outline with cell nuclei marked with asterisks. **(B–D)** Quantification of SC length (B), terminal branch length (C), and SC number (D) along singly innervating branches, showing no significant difference after BTX treatment in P9 *Plp*-GFP mice injected with BTX versus control (≥10 axons per animal in $n = 5$ mice). **(E and F)** Quantification of axonal SC length (E; din, 30 ± 2 µm; sin, 24 ± 1 µm) and terminal branch length (F; din, 50 ± 4 µm; sin, 54 ± 5 µm; ≥16 axons per animal in $n = 5$ mice). **(G)** Images of competing (din) and winner (sin) terminal branches in P9 Thy1-YFP16 mice, without or with emerging Caspr paranodes (green) and stained βIII-tubulin (white). **(H)** Quantification of βIII-tubulin intensity (x-fold normalized to Thy1-YFP16; Caspr negative, $n \geq 18$ axons per group in $n = 3$ mice). din, competing axons; sin, winner axons. Data represent mean + SEM. *, $P < 0.05$; **, $P < 0.01$; ***, $P < 0.001$; ns., not significant; Mann–Whitney test. Outlier determined by Tukey test. Scale bar, 10 µm (A and G).

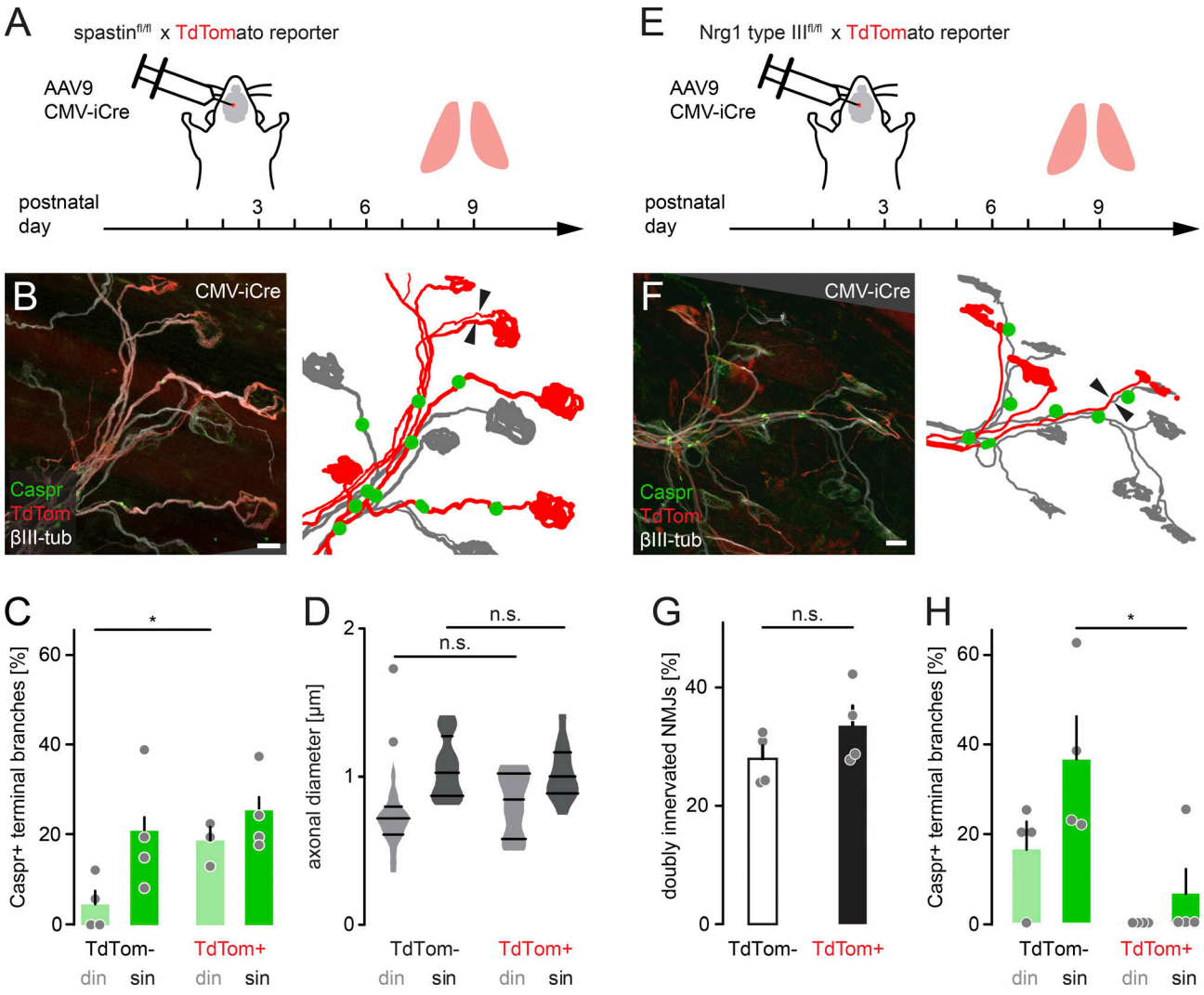

Figure S3. **AAV9-mediated spastin deletion promotes myelination on competing branches. (A)** Schematic of experimental design. AAV9-*CMV*-iCre was injected at P2 into the third ventricle of spastin$^{fl/fl}$ × TdTomato reporter mice. Muscles were analyzed at P9. **(B)** Image of P9 muscle immunostained for Caspr (green) and βIII-tubulin (white). iCre-mediated deletion resulted in TdTomato-positive axons (red), presumed to lack spastin. Schematic on the right depicts TdTomato-positive (red) and negative motor units (gray) and Caspr paranodes (green). Arrowheads point to competing axons leading to the same NMJ. **(C)** Quantification of Caspr immunostaining on TdTomato-negative and positive terminal branches at P9 ($n \geq 3$ mice per group, $n \geq 15$ axons per mouse). **(D)** Quantification of axon diameter of TdTomato-negative and positive terminal branches at P9 ($n \geq 10$ axons per group, $n = 5$ mice). **(E)** Schematic of experimental design. AAV9-*CMV*-iCre was injected at P2 into the third ventricle of Nrg1 type III$^{fl/fl}$ × TdTomato reporter mice. Muscles were analyzed at P9. **(F)** Image of P9 muscle immunostained for Caspr (green) and βIII-tubulin (white). iCre-mediated deletion resulted in TdTomato-positive axons (red), presumed to lack Nrg1. Schematic on the right depicts TdTomato-positive (red) and negative motor units (gray) and Caspr paranodes (green). Arrowheads point to two axons leading to the same NMJ. **(G)** Quantification of doubly innervated NMJs on TdTomato-negative and positive terminal branches at P9 ($n = 4$ mice per group, ≥97 axons per animal). **(H)** Quantification of Caspr immunostaining on TdTomato-negative and positive terminal branches at P9 ($n = 4$ mice per group, ≥29 axons per animal). din, competing axons; sin, winner axons. Data represent mean + SEM. *, $P < 0.05$; n.s., not significant; Mann–Whitney test. Outlier determined by Tukey test. Scale bar, 10 µm (B and F).

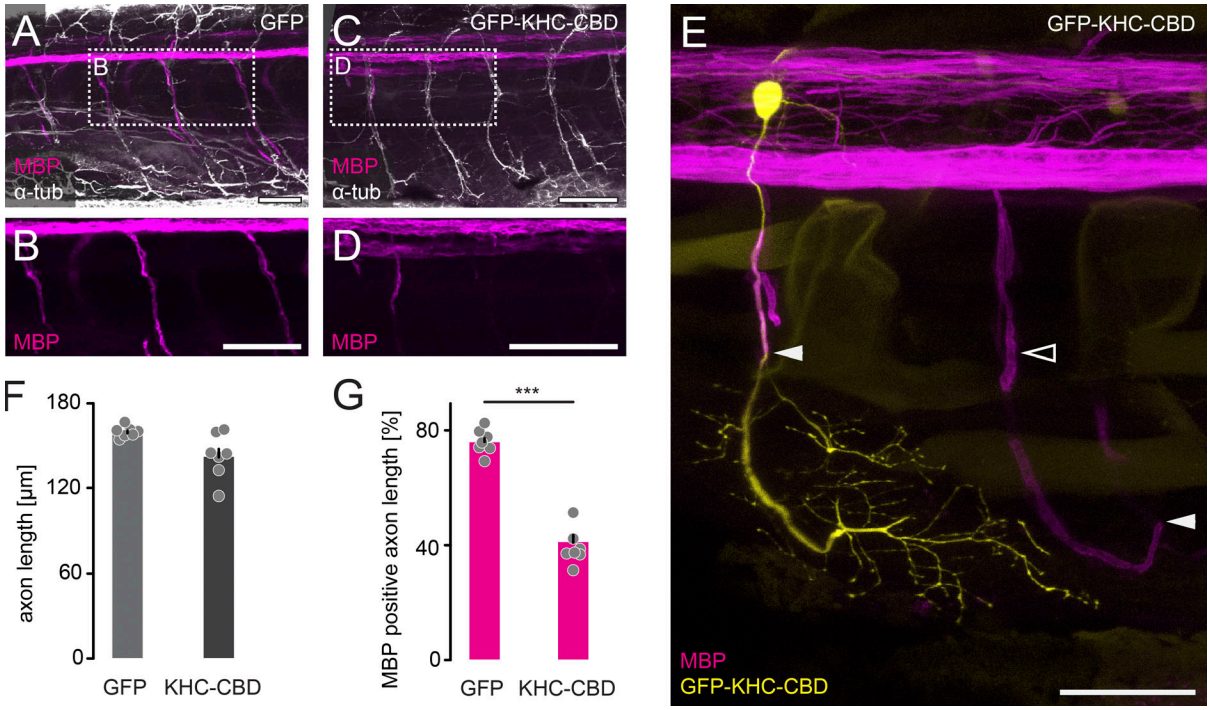

Figure S4. **Microtubule-dependent axonal transport affects myelination onset. (A–D)** Whole-mount immunohistochemical staining against α-tub (white) to label axons in Tg(mbp:RFP) (magenta) transgenic zebrafish larvae injected with cntn1b:GFP as control (A and B) and cntn1b:GFP-KHC-CBD (C and D). Dashed boxes in A and C are enlarged in B and D showing mbp:RFP only. **(E)** Example of an individual cntn1b:GFP-KHC-CBD–labeled motor neuron (yellow) and its myelination (magenta). Solid arrowheads point to ends of myelin sheaths; empty arrowhead points to extend of myelination along KHC-CBD–expressing axons compared with control axons in the adjacent somite (unlabeled). **(F)** Length of spinal motor axons, measured between the branching-off point at the spinal cord to the axon tip ($n = 7$ zebrafish per group, $n \geq 29$ axons per animal). **(G)** Progress of myelination expressed as percentage of mbp:RFP-positive axon length ($n = 7$ zebrafish per group, $n \geq 29$ axons per animal). Data represent mean + SEM. ***, $P < 0.001$, Mann–Whitney test. Scale bar, 50 µm (A–E).

Table S1 is provided online and lists the mouse lines and genotyping primers used.